1

Spatiotemporal soil fertility responses to an enhanced rock weathering deployment within a temperate, agricultural watershed

Quinn Zacharias[1], Robert Rioux[1], Fengchao Sun[1], Wyatt Tatge[1], Evelin Pihlap[2,3], Emmanuel Nyavor[4], David Foster[4], Joshua L. Warren[5], Mark A. Bradford[1], Peter Raymond[1,6], Noah Planavsky[7], James Saiers[1]

[1]Yale University, School of the Environment, New Haven, United States

[2]Swedish University of Agricultural Science, Department of Soil and Environment, Uppsala, Sweden

[3]Centre of Estonian Rural Research and Knowledge, Soil Science Unit, Tartu, Estonia

[4]University of Florida, Department of Geological Sciences, Gainesville, United States

[5]Yale University, Department of Biostatistics, New Haven, United States

[6]Yale Center for Natural Carbon Capture, New Haven, United States

[7]Yale University, Department of Earth and Planetary Sciences, New Haven, United States

Corresponding author: Quinn Zacharias, quinn.zacharias@yale.edu

16

Abstract

Enhanced rock weathering (ERW) is a promising strategy for removing carbon dioxide from the atmosphere, yet field-scale observations suitable for evaluating ERW co-benefits related to soil-fertility improvements within temperate agriculture settings remain scarce. We conducted a 2.5-year investigation within a headwater catchment at the Sleepers River Research Watershed in Danville, Vermont, applying 20 t ha^{-1} of finely milled, calcium-rich meta-basalt to near-stream pastures and adjacent, upslope hayfields. After establishing a year-long baseline, we continued to monitor topsoil chemical fertility indicators (pH, exchangeable essential nutrients, and cation exchange capacity) for 13 months following basalt application to evaluate changes relative to untreated control transects. The basalt amendment significantly raised soil pH by 0.15–0.24 units ($p < 0.05$) and increased exchangeable calcium by as much as 12%, with larger pH gains in soils that were initially more acidic. Other nutrients showed only modest responses, partly reflecting slow dissolution of metamorphic minerals rich in potassium and magnesium. Higher background variability in the pasture may have muted the detectable basalt-treatment signal, yet across the hillslope catena the magnitude of pH change scaled inversely with initial pH (lowest at the shoulder and foot), illustrating the role of land use and topographic position in modifying ERW responses. These results indicate that calcium-rich meta-basalt acts as a slow-release liming agent in well-buffered temperate soils and provide indications of the co-benefits of ERW to improving soil health within temperate agroecosystems.

Introduction

Enhanced rock weathering (ERW) is emerging as a promising carbon sequestration strategy that could capture gigaton-scale quantities of carbon dioxide (CO_2) from the atmosphere

39 while providing agricultural co-benefits (Beerling et al., 2020; Holzer et al., 2023; Larkin et al.,

40 2022). The technique accelerates the natural weathering of silicate minerals by grinding rock to

41 increase surface area and spreading this feedstock across cropland. When the feedstock interacts

42 with soil water, its constituent minerals dissolve in response to acids in the soil solution.

43 Carbonic acid, produced when atmospheric CO_2 dissolves in infiltrating soil water and when

44 roots and soil microbes respire CO_2 into soil pores, is responsible for carbon sequestration.

45 Dissolution of the minerals consumes acidity and generates bicarbonate ions (HCO_3^-) that may

46 travel with soil water and shallow groundwater to surface waters and ultimately to the ocean,

47 where they contribute to longer-term carbon storage (Hartmann et al., 2013).

48   Beyond carbon sequestration, ERW can improve soil fertility by increasing nutrient

49 availability and altering soil physicochemical properties. Weathering of silicates also releases

50 phosphorus (P), potassium (K), calcium (Ca), and magnesium (Mg); these dissolution products

51 can be taken up by plants directly or adsorbed by soil minerals and organic matter, improving the

52 balance of nutrients available to crops (Moretti et al., 2019; Swoboda et al., 2022). By

53 neutralizing acidity and promoting the formation of secondary clays and metal oxides, ERW can

54 increase the soil's permanent cation exchange capacity. Raising soil pH leads to deprotonation of

55 surface-functional groups on existing mineral and organic matter surfaces (predominantly

56 carboxyl groups), expanding the pool of exchange sites available under field conditions (Gillman

57 et al., 2002; Ross & Ketterings, 1995; te Pas et al., 2023). These shifts in soil chemistry have the

58 potential to increase yields and the nutrient content of harvested crops, delivering tangible

59 benefits to farmers and consumers (Burbano et al., 2022; Luchese et al., 2021; Ramos et al.,

60 2020).

61   Crushed silicate rocks have been used intermittently as soil amendments for decades

62   (Barbier et al., 2021; Plucknett, 1972; Wolf & Heard, 1983; Yusiharni et al., 2007). Positive

63   effects on soil pH and nutrient availability are most commonly observed in tropical soils or at

64   high application rates (Dahlin & Stenberg, 2017; Gunnarsen et al., 2019; Manning et al., 2017;

65   Tavares et al., 2018). Responses tend to be smaller in temperate regions (Campbell, 2009; Dupla

66   et al., 2023; Ramezanian et al., 2013). This contrast has been attributed to lower weathering rates

67   in cooler climates and also reflects that many temperate soils are better buffered, more saturated

68   with base cations and inherently richer in nutrients than their tropical counterparts (Burbano et

69   al., 2022). Although application rates of 50–250 t ha^{-1} have induced measurable changes in soil

70   chemistry in temperate field trials (Beerling et al., 2024; Dahlin & Stenberg, 2017; Vienne et al.,

71   2022), such rates exceed typical agronomic practice. Studies exploring more moderate rates

72   appropriate for on-farm deployment remain relatively few.

73   While ERW is recognized for delivering agronomic co-benefits to soil health, notably

74   raising soil pH and supplying essential nutrients (Cong et al., 2024), its soil fertility outcomes

75   likely vary widely across heterogeneous field conditions (Blette & Newton, 1996). Differences in

76   topographic position and land use create a mosaic of baseline acidity and nutrient availability

77   that could modulate soil responses to basalt amendment (Aksoy & Kavvas, 2005; Wang et al.,

78   2023). Accordingly, we evaluate changes in standard soil fertility indicators, which are routinely

79   measured in the region to guide liming and fertilizer recommendations, including soil pH, cation

80   exchange capacity, and exchangeable essential macronutrients (Ca, Mg, K, and P) following

81   basalt application across these varied field contexts. Our experimental design spans an upland

82   hillslope catena encompassing both hayfields and pastures, thereby capturing inherent gradients

83   in initial soil acidity and nutrient status along slope positions and between land uses.

84 Furthermore, whereas most ERW field trials incorporate rock dust via tillage (Beerling et al.,

85 2024; Haque et al., 2020; Kantola et al., 2023), we applied basalt as a surface top-dressing

86 (without mechanical incorporation), a scalable yet less well-studied approach that avoids soil

87 disturbance. Our objectives are to identify which indicators respond most strongly to basalt

88 application, to characterize how treatment effects evolve over time and to evaluate whether

89 responses vary with land use (hayfield versus pasture) and hillslope position within those land

90 uses. Addressing these questions will advance understanding of ERW's agronomic co-benefits

91 and inform management strategies for temperate agroecosystems.

Methods

92

Site description

93

94 In June 2023, finely ground meta-basalt was surface-applied at a rate of 20 t ha^{-1} with a

95 tractor-pulled lime spreader across 15% of a 59-ha agricultural watershed (Fig. 1). This

96 watershed (Watershed 2, hereafter W2) lies within the Sleepers River Research Watershed in

97 northern Vermont (44°27′28″ N, 72°05′31″ W; elevation 300 m). The region has a mean annual

98 temperature of 5.7 °C and receives 100–150 cm of precipitation annually, of which 25–30%

99 typically falls as snow . The subsurface geology comprises 3–10 m of glacial till overlying the

100 Waits River Formation, and the terrain is characterized by 10–20% hillslope gradients forming a

101 typical catena soil pattern (Sun et al., 2025). According to USDA soil maps, the topsoil in W2 is

102 classified as Cabot loam. Hydrometer analyses indicated that the upland hayfield soil, based on a

103 composite sample from 32 plots, was a sandy loam (sand 51%, silt 39%, clay 11%), whereas the

104 downslope pasture soil, from 32 plots, was a loam with roughly equal sand and silt fractions

105 (sand 45%, silt 45%, clay 11%). Exploratory soil pits in the lower pasture and upper hayfield

106   revealed a consistent granular structure in the A horizon extending to ~15–20 cm depth (Table

107   S1, Fig. S1). Subsurface profiles showed leaching in the hayfields and secondary accumulation

108   of Ca^{2+} and Mg^{2+} in the pastures (Table S1, Fig. S1). Vegetation within the watershed is

109   dominated by orchard grass (*Dactylis glomerata*), planted as a monocrop around 2000,

110   interspersed with tall fescue (*Festuca arundinacea*), reed canary grass (*Phalaris arundinacea*),

111   Kentucky bluegrass (*Poa pratensis*), red clover (*Trifolium pratense*), and white clover (*Trifolium*

112   *repens*), with verified specimens archived at the yale herbarium (Yale Herbarium, 2023). The

113   upper fields are managed for hay production, while the lower fields support rotational grazing of

114   dairy and beef cattle from May through October each year (Fig. 1).

115

116
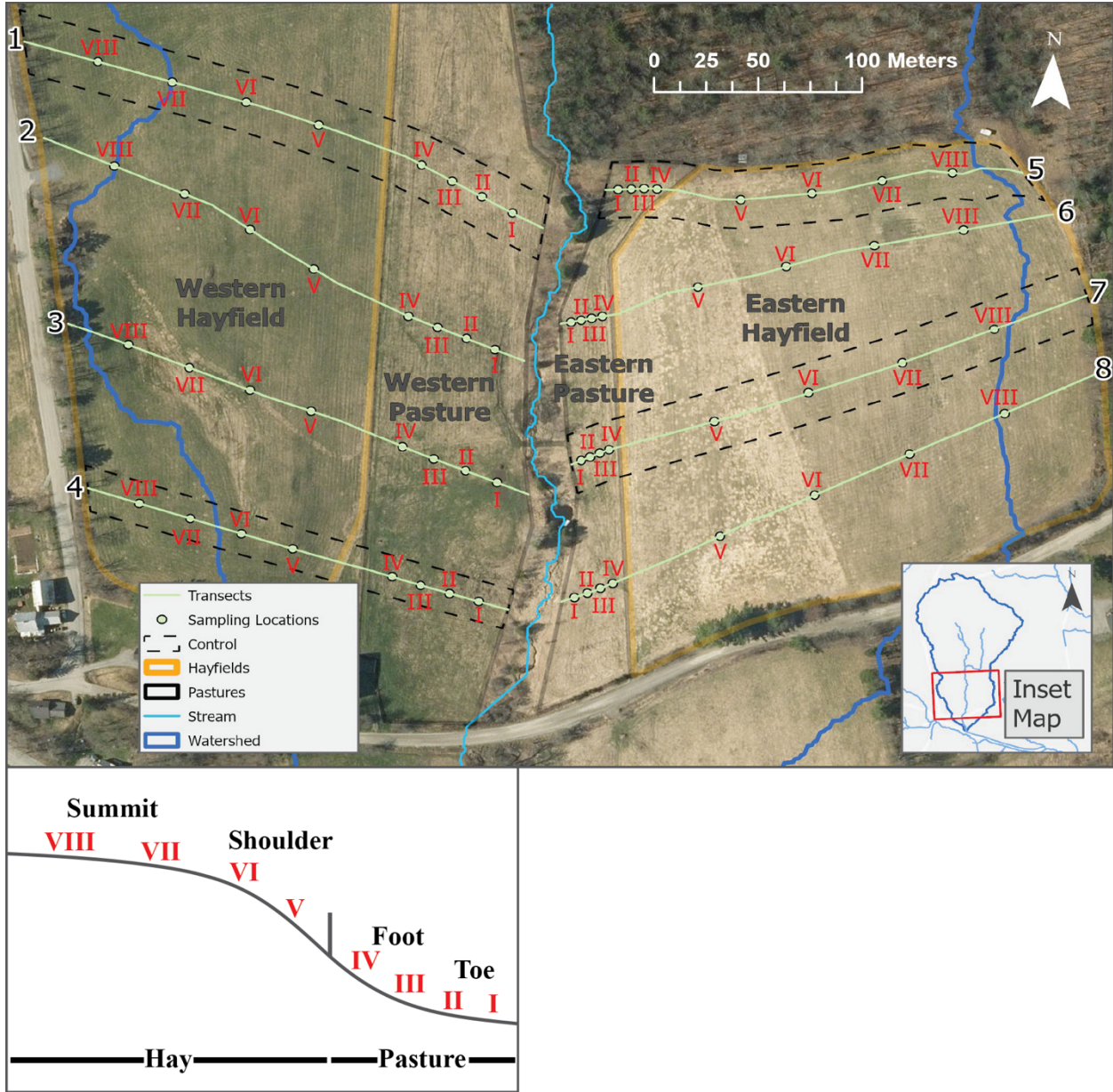
Fig. 1. Map of the ~ 59 ha, first-order agricultural watershed in northern Vermont (Watershed 2 [W2]), showing the experimental layout. Four enclosed fields are delineated by their land use, western and eastern pastures (outlined in thin black) and western and eastern hayfields (outlined in pale yellow), separated by a fenced riparian corridor. Eight transects (labeled 1–8) run parallel to the hillslope gradient from the lower slopes (near the riparian zone) to the upland field edges; four transects are designated as controls (bracketed by dashed black lines) and four received basalt treatments (solid lime green lines without dashed lines). At each transect, soil-sampling plots are shown as lime green dots labeled with red Roman numerals (I–VIII), starting at I near the toe slope and increasing upslope to VIII. Within each fenced field, these sampling plots are spaced evenly between the fence boundaries. The blue line traces the stream as it flows through the watershed, whose boundary is shown in dark blue. The inset map (lower right) situates the experimental layout within W2. The schematic cross-section beneath the aerial map traces the hillslope catena along a typical sampling transect, showing the eight sampling plots (I–

130 VIII) stepping upslope from the pasture toe-slope (plots I, II) and foot-slope (plots III, IV) through the
131 fence line into the hayfield shoulder (plots V, VI) and summit (plots VII, VIII).

132

Experimental and sampling design

134   Eight transects were established across the watershed, with four positioned on each side

135 of the central stream and oriented parallel to the hillslope (Fig. 1). Four treatment transects

136 received crushed basalt, while four control transects were embedded within 30-m wide basalt-

137 exclusion strips. Each transect included four evenly spaced sampling plots in the pasture and four

138 in the adjacent upslope hayfield. Transects 1, 4, 5, and 7 served as controls, while transects 2, 3,

139 6, and 8 received the crushed basalt amendment. The transects were originally planned to

140 alternate between control and treatment, but we altered this arrangement on the western side of

141 the stream because transect 3 lay within a hollow making it susceptible to basalt runoff from

142 adjacent plots. This design yielded 64 sampling plots in total, capturing a range of hillslope

143 positions under two land uses while interspersing control and treatment plots across the

144 landscape (Fig. 1). The experimental layout, together with the timing of soil sampling relative to

145 the basalt application (see below), followed a before–after, control–impact (BACI) framework

146 and allowed data to be aggregated by treatment status and landscape position.

147   Baseline topsoil samples (0–15 cm depth) were collected in fall 2022 (September–

148 October) and again in spring 2023 (March–April) prior to basalt application. Fall and spring

149 were chosen because farm operations were minimal then. The basalt was applied in June 2023,

150 and post-treatment soil sampling was conducted at the same plot locations in fall 2023,

151 spring 2024, and fall 2024 to track temporal changes in soil chemical properties. For the initial

152 baseline (fall 2022), three cores of 5 cm diameter were taken per plot and composited. In all

153 subsequent sampling events, eight cores of 1.59 cm diameter were taken per plot, then combined

154 and homogenized in the field. All samples were air-dried in paper bags at 22–24 °C and 30–35%

155 relative humidity for one week. After drying, samples were passed through a 2 mm sieve and

156 homogenized. Coarse roots greater than 1-mm in diameter were removed prior to chemical

157 analysis.

Feedstock description

159 The amendment was a finely ground, Ca-rich meta-basalt ("Pioneer Valley Basalt")

160 sourced from a quarry in western Massachusetts. The material had a BET surface area of 4.29 m²

161 g^{-1} and a gravimetric moisture content of $10.1 \pm 0.2\%$. Mineralogy was dominated by plagioclase

162 and clinopyroxene with about 25–30% of the primary minerals converted to metamorphic and

163 alteration phases. Full oxide composition, mineralogy, grain size distribution, and extractable

164 nutrients are provided in the supplemental information (Table S2a–S2c; Figs. S2–S3).

Soil chemical analysis

166 Soil fertility parameters were quantified through standard chemical assays on both

167 unamended soil and soil–basalt mixtures after treatment. We focused on pH, effective cation

168 exchange capacity, and the essential macronutrients Ca, Mg, K, and P, which together,

169 commonly form the chemical core of routine soil fertility tests used by farmers and extension

170 services to guide lime and manure applications. Nitrogen (N) and sulfur (S) were excluded from

171 this essential macronutrient suite, because they are not typically supplied by basalt, though they

172 can be supplied via other amendments (Amgain et al., 2021). Additions of these Soil pH was

173 measured in a 1:1 (v/w) slurry of air-dried soil and deionized water, following standard protocols

174 for moderately acidic New England soils. Plant-available nutrients were extracted using a

175 modified Morgan solution (0.62 N NH₄OH + 1.25 N CH₃COOH, buffered to pH 4.8). For each

176 extraction, 20 mL of the modified Morgan solution was added to 4.0 g of soil (a 1:5 solution:soil

177 ratio) in a centrifuge tube and shaken at 180 rpm for 15 minutes. The suspension was then

178 filtered through medium-porosity filter paper (Whatman No. 2), and the filtrate was retained for

179 analysis. Phosphorus in the extract was determined colorimetrically by flow injection analysis,

180 while all other extracted nutrients and metals were measured by ICP–OES. Soil organic matter

181 (OM) was determined by loss-on-ignition, in which air-dried subsamples were oven-dried at

182 105 °C for 2 h, ignited at 360 °C for 2 h, and OM (%) calculated from mass loss using a regional

183 calibration equation (Northeast Soil Testing Procedures, Cooperative Bulletin 493).

184   Effective cation exchange capacity (ECEC) was estimated by methods appropriate for the

185 soil pH. In soils with pH > 6, ECEC was taken as the sum of exchangeable base cations

186 $(Ca^{2+} + Mg^{2+} + K^+ + Na^+)$ (Ross & Ketterings, 1995). In more acidic soils (pH ≤ 6), exchangeable

187 acidity $(H^+ + Al^{3+})$ was also included in the total. Exchangeable acidity was quantified using the

188 Mehlich buffer pH method, which utilizes measurements of the soil pH in water (pH_water) and

189 the pH of a soil–buffer mixture after 30 minutes of equilibration (pH_buffer). These

190 measurements were then applied to an empirical calibration equation derived from a regional soil

191 incubation study (Hoskins & Ross, 2009) to compute exchangeable acidity in units of meq per

192 100 g^{-1} of soil:

193 $$EA = 20.1 - (0.88 \times pH_{water}) - (2.46 \times pH_{buffer\ soln}) \qquad (1)$$

194 ## Statistical analyses

195   We used linear mixed-effects (LME) regression to evaluate the effects of basalt treatment

196 on each soil fertility variable. Separate LME models were fit for the pasture plots and the

197 hayfield plots because diagnostic residual plots indicated different variance patterns between

198   these two land-use groups. Both models were identical in structure and accounted for basalt

199   treatment effects, which could vary with time, and hillslope position effects, as well as

200   interactions among these factors. For the pasture model, hillslope position was treated as a

201   categorical factor with two levels: toe slope (plots I, II) vs. foot slope (plots III, IV), with the foot

202   slope designated as the reference position. For the hayfield model, the position factor was

203   shoulder slope (plots V, VI) vs. summit (plots VII, VIII), with the summit designated as the

204   reference position. (See Fig. 1 for plot locations along the hillslope.) All models incorporated a

205   random intercept for each plot (within each transect) to account for plot-to-plot differences and

206   the repeated measurements over time. Taken together, this modeling framework evaluates basalt

207   effects across four slope–land-use categories: pasture toe, pasture foot, hayfield shoulder, and

208   hayfield summit. Each model was based on ~180 observations (182 for hayfield, 183 for

209   pasture). The LME regression is given as

210    $$Y_{ijt} = \mu + x_{ij}\beta + 1(t = 2)\eta_2 + \sum_{t^*=3}^{5} 1(t = t^*)\{\eta_{t^*} + z_{it^*}(\alpha_{t*} + x_{ij}\delta_{t*})\} + \phi_{ij} + \epsilon_{ijt} \quad (2)$$

211

212   where Y_{ijt} is the soil-chemistry measurement at plot j within transect i at time t, μ is the expected

213   value of Y at sampling time $t^* = 1$ at the reference hillslope position, x_{ij} is a binary variable

214   indicating if plot j within transect i is in the non-reference hillslope position, β is hillslope effect

215   relative to the reference position, z_{it^*} is a binary variable indicating if transect i at sampling time

216   t^* is treated or not, η_{t^*} are time fixed effects, α_{t*} quantifies the basalt-treatment impact at the

217   reference hillslope position for $t^* = 3$, 4, and 5, $\delta_t{}^*$ quantifies basalt-treatment impact relative to

218   the reference hillslope position for these sampling times, ϕ_{ij} is the random intercept for plot j

219   within transect i, and ϵ_{ij} is the residual error.

220   The regression-model parameters were estimated from soil-fertility measurements made

221   two times prior to the basalt application and three times following basalt application. The

222   estimates of α_{t*} and $\alpha_{t*} + \delta_{t*}$ are of greatest interest because these quantify the effects of

223   interactions between basalt treatment and hillslope position on soil-fertility variables. In our

224   formulation, the basalt-treatment effect at the reference hillslope position (foot slope in pastures

225   or summit in hayfields) at a given post-treatment time is denoted by α_{t*}, while the effect relative

226   to the reference at the lower hillslope position (toe slope in pastures or shoulder slope in

227   hayfields) at that time is denoted by δ_{t*}. Thus, for each post-application sampling ($t* = 3, 4, 5$

228   corresponding to fall 2023, spring 2024, fall 2024), the treatment effect in the lower-slope plots

229   is ($\alpha_{t*} + \delta_{t*}$), while in the upper-slope plots it is α_{t*}. The model also incorporates time fixed-

230   effects ($\eta_2, \eta_3, \eta_4,$ and η_5) to control for unobserved factors that may vary with time and are

231   common to the sampling plots.

232   All statistical analyses were conducted in R (v4.4.1) using the nlme package. Prior to

233   modeling, all response variables except pH were $\log_e$-transformed to improve normality and

234   homoscedasticity of residuals; diagnostic Q–Q plots and residual-versus-fitted plots confirmed

235   that this transformation was effective. Although pH is a logarithmic function of hydrogen ion

236   concentration, we analyzed acidity both on the pH scale and, where appropriate, in terms of $[H^+]$

237   to confirm that model interpretations were consistent across linear and logarithmic

238   representations. Variogram analysis of the LME residuals indicated no appreciable spatial

239   autocorrelation, suggesting that the inclusion of plot-level random intercepts adequately

240   accounted for any location-based dependencies in the data. We considered effects statistically

241   significant at $\alpha = 0.05$ and marginally significant at $0.05 < p < 0.1$. We used Wald tests to

242   evaluate the significance of specific linear combinations of fixed-effect parameters that

243 correspond to the basalt-treatment effect at each hillslope position. For example, tests on $\alpha_3 + \delta_3$,

244 $\alpha_4 + \delta_4$, and $\alpha_5 + \delta_5$ assessed whether the basalt had a significant impact on a given soil variable

245 at the lower-slope positions in fall 2023, spring 2024, and fall 2024, respectively. To facilitate

246 interpretation of model coefficients, we back-transformed the estimates from the log-scale

247 models to express effect sizes as percentage changes in the original units. For instance, a fixed-

248 effect coefficient c obtained for a $\log_e$-transformed variable was converted to an estimated

249 change of $[(e^c - 1) \times 100]\%$ in the untransformed variable associated with that effect. This

250 approach allowed us to discuss the influence of the basalt amendment in terms of relative

251 changes (percent increase or decrease) in soil fertility metrics under field conditions.

Results

Overview of baseline soil chemistry

254 Soil samples were collected prior to basalt application in fall 2022 and spring 2023 from both

255 control and treatment transects. The median pH (across 64 sites for the two sampling times)

256 equaled 6.1, and pH at individual plots ranged from 4.9 to 7.7, with the highest values of pH

257 occurring in pasture sites of transect 1 (Table S3a). ECEC varied from 4.4 to 22.4 meq 100 g^{-1}

258 with a median of 9.4 meq 100 g^{-1}. Base-cation saturation was high, exceeding 73% for all soil

259 samples and averaging 95%. Calcium ions dominated base saturation, contributing to 86% of the

260 total exchangeable bases on average (Table S3). Magnesium ions comprised 10% of the base-

261 cation pool on average, with the remaining 5% was attributable to the sum of K^+ and Na^+. OM

262 was similar in the hayfield (6.9%) and pasture (6.5%) soils (Table S1).

Hillslope catena (baseline conditions)

In fall 2022, median pH equaled 5.8 along the pasture toe slope, decreased to a minimum value of 5.6 at the foot slope, and increased to 6.4 along the shoulder slope and summit of the upgradient hayfield (Table S3a; Fig. 2). Base saturation varied similarly with hillslope position, although median values exhibited small variation across hillslope position ranging from 90 to 98%. Median concentrations of Ca^{2+} also increased on both sides of the foot slope, varying from 1,009 mg kg^{-1} at this hillslope position to a maximum of 1,833 mg kg^{-1} at the summit (Table S3a; Fig. 2). The median concentration of Mg^{2+} deviated from this spatial pattern, although it did exhibit its greatest increase across the pasture-to-hayfield transition in a consistent fashion with pH, base saturation, and Ca^{2+}. Whereas median values of Ca^{2+} and Mg^{2+} were greater in the upslope hayfield positions than in the pasture, those for K^+ exhibited the opposite relationship (Table S3a) and were approximately 2-fold greater along the pasture foot slope than along the hayfield summit. Soil P concentrations had a median of 1.2 mg kg^{-1} at the toe-slope and foot-slope plots of the pasture, which was 33% lower at both the shoulder and summit positions within the hayfield. Baseline LME models (Tables S4a–S4f) confirmed that in the pasture, slope position significantly predicted pH, Ca^{2+}, and ECEC ($p < 0.05$), whereas in the hayfield, slope effects were weaker and generally nonsignificant. In these models, the slope coefficient (β) quantifies the mean difference between the lower and upper slope positions relative to the reference position (foot slope in pasture, summit in hayfield), while the time (seasonal) term (η_2) represents changes between the fall 2022 and spring 2023 baseline samplings. Seasonal fixed effects captured additional variation in Mg^{2+} and P, though the magnitude of these temporal shifts was small. We present descriptive summaries here for clarity, with full model outputs provided in the SI.

286   The hillslope patterns in soil-fertility variables observed in fall 2022 were preserved in

287   spring 2023 (Table S3b, Fig. 2), and the fall to spring changes in pH and elemental

288   concentrations between the baseline sampling times were generally small. Median pH, for

289   example, increased by 0.1 units at the toe slope and decreased by 0.2 units at the shoulder slope

290   and summit while remaining unchanged at the foot slope. The greatest fall to spring change

291   involved Ca^{2+}, which increased by 42% at the toe-slope plots, but changed by less than 10%

292   along the remaining hillslope positions.
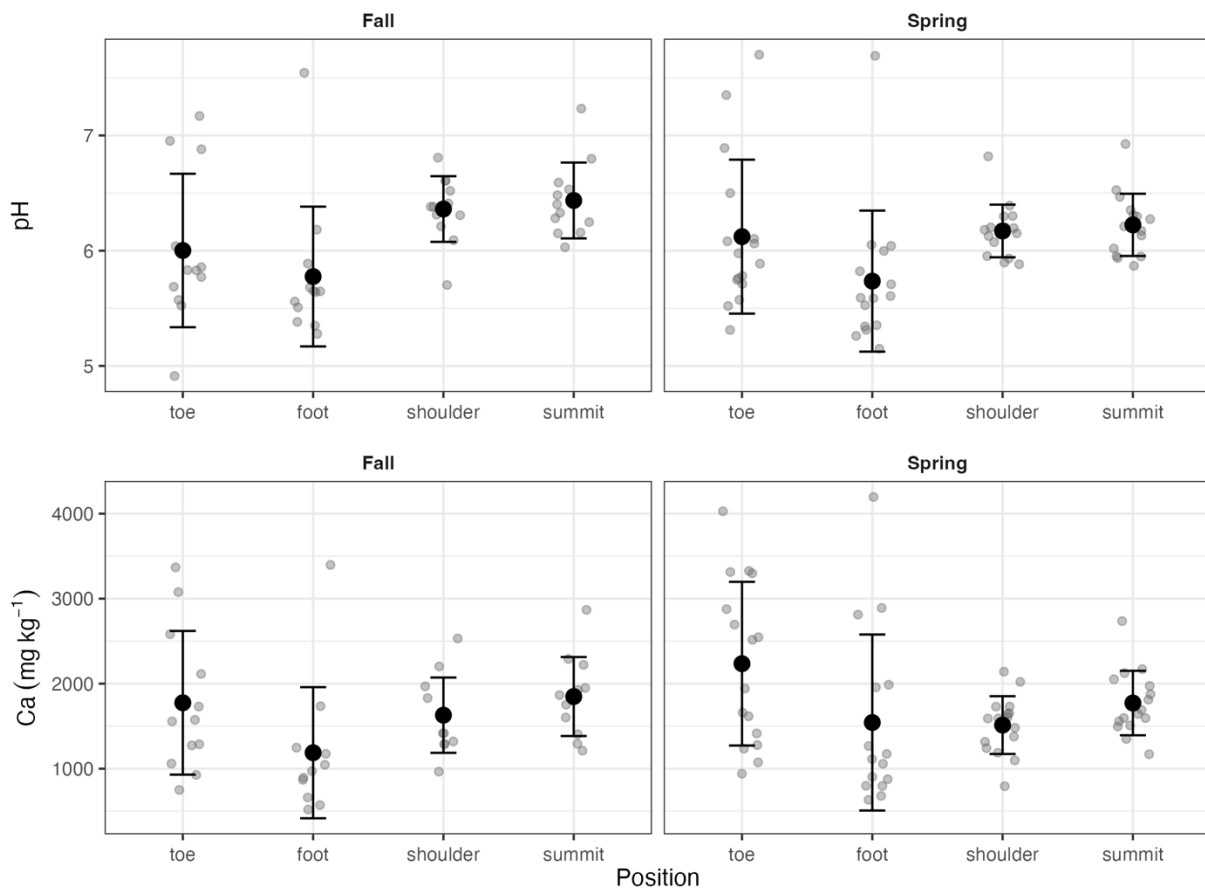
293

294   **Fig. 2.** Pre-application mean pH (top) and exchangeable Ca^{2+} (bottom) across hillslope positions in fall
295   (left) and spring (right). Black points are group means (± standard error), grey dots individual
296   observations.

Field-level effects of enhanced rock weathering

Hayfield

Soil pH responded most strongly to the basalt treatment (Table 1). Estimates of the basalt-treatment impacts on pH along the summit (α_3, α_4, α_5) increased for all post-application sampling times. The greatest pH increase, 0.15 units (~30% lower [H^+]), occurred during spring 2024 and was statistically significant, while the smaller increases in fall 2023 (0.10 units) and fall 2024 (0.03 units) were not. The pH response on the shoulder slopes, as quantified by α_{t*} + δ_{t*}, was more pronounced than on the summits (Table 1). Along the shoulder slopes, increases in pH attributable to the basalt addition ranged from 0.15 (~30% lower [H^+]) to 0.21 units (~39% lower [H^+]), and these effect sizes were statistically significant for all post-application sampling times. Modest increases in Ca^{2+} along the shoulder plots, varying from 6 (insignificant) to 12% (significant), were also associated with the basalt addition. Basalt-attributable changes in Ca^{2+} were smaller for summit plots and statistically insignificant. The basalt treatment was generally, but not always, associated with lower soil Mg^{2+} and K^+ concentrations, although significant effects, equaling −11% for Mg^{2+} and −25% for K^+, were observed only on the shoulder slopes in fall 2023 (Table 1). Lower soil P concentrations were similarly associated with the basalt amendment. The significance of this association was restricted to summit positions during the second and third post-application sampling times when P concentrations for an average basalt-treated plot were 23% to 29% lower than for an average control plot. Changes in ECEC following basalt treatment were small (−5% to 8%) and not statistically significant.

Table 1. Change in soil pH and percent change in Ca^{2+}, Mg^{2+}, K^+, P, and ECEC in response to basalt treatment in the Hayfield. Bolded values are statistically significant at $p < 0.05$. Times 3, 4, and 5 correspond to fall 2023, spring 2024, and fall 2024, respectively. See Tables S4a–S4f for full model results.

Parameter	Parameter Definition	pH	ECEC (%)	Ca^{2+} (%)	Mg^{2+} (%)	P (%)	K^+ (%)

α_3	Treatment, summit, Fall 23	0.10	2.1	2.9	−3.1	−16.3	−12.8
α_4	Treatment, summit, Spr 24	**0.15**	−4.6	−5.0	−5.5	**−22.8**	9.9
α_5	Treatment, summit, Fall 24	0.03	−4.0	−4.7	−3.7	**−29.2**	5.4
$\alpha_3 + \delta_3$	Treatment, shoulder, Fall 23	**0.21**	7.6	**12.0**	**−11.3**	−1.0	**−24.8**
$\alpha_4 + \delta_4$	Treatment, shoulder, Spr 24	**0.15**	7.0	9.1	2.7	15.8	−3.8
$\alpha_5 + \delta_5$	Treatment, shoulder, Fall 24	**0.16**	4.5	6.3	−2.3	10.4	−11.0

Pasture

The basalt treatment appeared to increase soil pH within the pasture, and the size of this effect grew with time (Table 2). Based on estimates of α_3, α_4, and α_5, the basalt addition increased soil pH along the foot slope by 0.07, 0.19, and 0.24 units in fall 2023, spring 2024, and fall 2024, respectively. While the pH effect was statistically insignificant for the initial post-application sampling, it was marginally significant in spring 2024 (p = 0.08), corresponding to a ~36% reduction in hydrogen ion concentration, and significant in fall 2024 (p = 0.03), corresponding to a ~42% reduction. The basalt effect on pH for the toe-slope plots (i.e., $\alpha_{t*} + \delta_{t*}$) followed the same temporal trend and increased by 0.20 units in fall 2024, a marginally significant effect (p = 0.06) corresponding to ~37% lower [H$^+$] relative to baseline. Increases in Ca^{2+} along the foot slope attributable to the basalt addition were small and insignificant for all post-application time periods, ranging from 1 to 6%. The effect of basalt was to decrease Ca^{2+} concentrations at the toe slope, but these changes were similarly insignificant (Table 2). The response of Mg^{2+} to the basalt addition was qualitatively consistent with that of Ca^{2+}, exhibiting positive associations along the foot slope and negative associations on the toe slope, yet the effect sizes across all time periods were insignificantly not different from zero. Concentrations of K$^+$ and P also responded weakly to the basalt addition except at the toe-slope position in spring 2024, when the estimated percent change attributable to the treatment equaled −22% for both analytes.

342 **Table 2.** Change in soil pH and percent change in Ca^{2+}, Mg^{2+}, K^+, P, and ECEC in response to basalt
343 treatment in the pasture. Bolded values are statistically significant at $p < 0.05$. Times 3, 4, and 5
344 correspond to fall 2023, spring 2024, and fall 2024, respectively. See Tables S4g–S4l for full model
345 results.

Parameter	Parameter Definition	pH	ECEC (%)	Ca^{2+} (%)	Mg^{2+} (%)	P (%)	K^+ (%)
α_3	Treatment, foot, Fall 23	0.07	2.3	5.5	12.2	5.4	2.8
α_4	Treatment, foot, Spr 24	0.19	−0.4	4.7	18.1	−6.6	−15.5
α_5	Treatment, foot, Fall 24	**0.24**	−3.9	1.0	12.2	−12.2	−13.1
$\alpha_3 + \delta_3$	Treatment, toe, Fall 23	0.07	−4.4	−4.1	−7.6	−4.8	−10.1
$\alpha_4 + \delta_4$	Treatment, toe, Spr 24	0.17	−15.5	−13.9	−10.1	−22.3	−22.2
$\alpha_5 + \delta_5$	Treatment, toe, Fall 24	0.20	−5.4	−5.8	1.4	−17.1	1.5

346

Baseline Acidity Predicts Magnitude of Soil Chemical Response

348   Baseline soil acidity was strongly associated with the magnitude of the basalt-induced pH

349 change (Figure 3). There was a clear inverse correlation between initial pH and the subsequent

350 change in pH (ΔpH), such that more acidic soils (lower pre-treatment pH) experienced larger

351 increases in pH one year after basalt application. This relationship was even stronger when

352 expressed on a linear hydrogen-ion scale: soils with higher initial $[H^+]$ underwent the greatest

353 decreases in $[H^+]$ concentration ($\Delta[H^+]$) following treatment. Both metrics showed statistically

354 significant correlations (Pearson's *r* with 95% confidence intervals are given in Fig. 3),

355 illustrating that the most acidic sites had the largest pH responses, whereas initially near-neutral

356 soils changed very little.

357
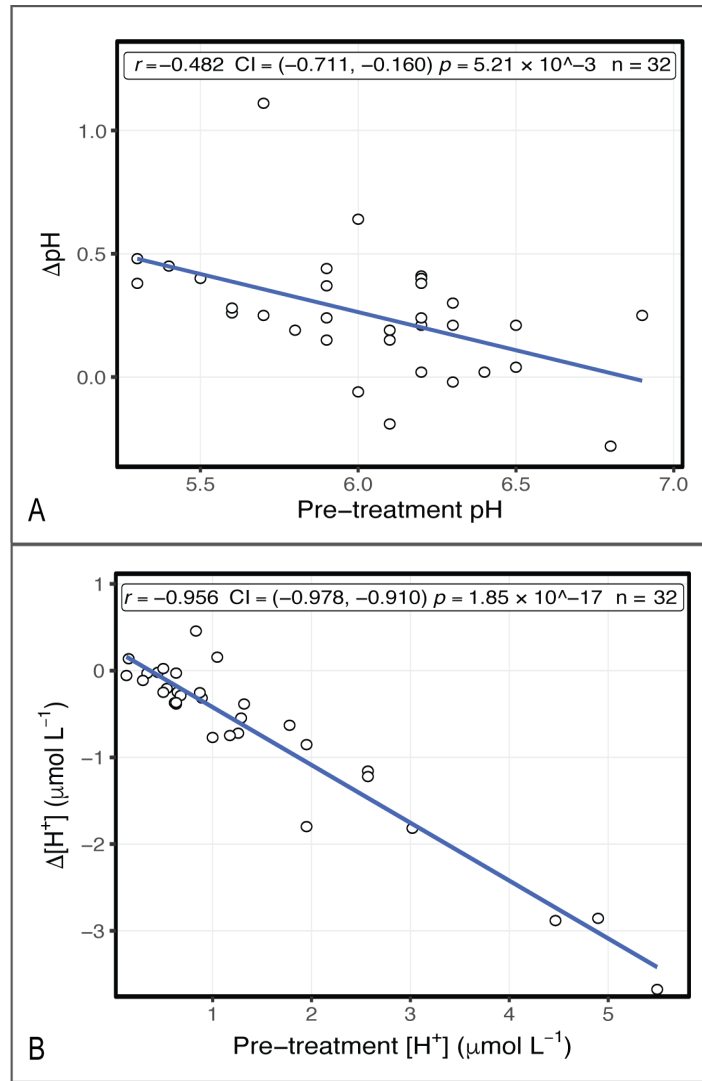
Fig. 3. Relationship between pre-treatment soil acidity and basalt-induced changes one year after application. (A) ΔpH versus initial pH. (B) $\Delta[H^+]$ versus initial $[H^+]$. Pearson's r, 95% CI, and p-values are shown within panels.

Discussion

Soil-chemical responses to basalt amendment

The basalt amendment primarily increased soil pH (0.15–0.24 units). These changes are consistent with measurements made in other temperate systems. For example, a 50 t ha^{-1} application of crushed basalt to an upland hay meadow led to 0.25-unit increase in soil pH (Bell et al., 2024). Similarly, a 0.2–0.3 unit increase in the pH of soils beneath a spring oat system was observed following an 18.6 t ha^{-1} basalt treatment (Skov et al., 2024). Under more acidic conditions, similar doses can produce larger pH shifts: a 0.45-unit increase at 20 t ha^{-1} was reported in a cocoa pot experiment (Anda et al., 2013), and 0.4–0.5-unit increases were observed with only 3.5 t ha^{-1} of dunite in a maize pot experiment (Moretti et al., 2019). Our comparative literature analysis shows that highly weathered tropical soils often experience greater acidity mitigation than temperate soils at similar basalt doses (Table S5).

The increase in soil pH likely results from the gradual dissolution of basalt, which releases alkalinity (as HCO_3^-) and base cations such as Ca^{2+} and Mg^{2+} (Lewis et al., 2021). These dissolution products raise soil-water pH, deprotonate variable-charge exchange sites, and neutralize soil acidity by displacing H^+ and Al^{3+} with base cations (Kauppi et al., 1984; Nagy & Kónya, 2007). Although multiple basalt-derived base cations may participate in exchange reactions, Ca^{2+} may preferentially occupy pre-existing and newly formed pH-dependent exchange sites. This preference could arise from (i) Ca^{2+}'s relatively low hydration energy and favorable exchange affinity, (ii) the potential incorporation of Mg^{2+} into newly forming secondary clay minerals (Nahon et al., 1982; Yan et al., 2021), and (iii) the preferential siting of Mg^{2+} in metamorphic actinolite and chlorite, which dissolve from the basalt more slowly than the original igneous silicate minerals. The modest pH increases we observed reflect the baseline

385   soils' low exchangeable acidity (Table 1), leaving little acidity to neutralize. Soils with the

386   lowest baseline pH and greatest exchangeable acidity, such as those at the foot slope, tended to

387   exhibit the largest pH changes (Tables 1–2; Tables S3a–S3b). Moreover, a clear inverse

388   relationship between baseline pH and pH change illustrates that more acidic soils exhibited

389   greater pH shifts (Figure 3). These patterns indicate a shift in the dominant mechanism: in

390   neutral soils, pH increases stem primarily from bicarbonate addition, whereas in acidic soils,

391   displacement of H^+ and Al^{3+} from the exchange complex is more important. Thus, acidic soils

392   exhibit larger pH increases while neutral soils change little, illustrating how soil buffering

393   capacity and chemical equilibria shape the pH response to basalt amendment (Kauppi et al.,

394   1984; Skov et al., 2024).

395   Basalt application modestly increased exchangeable Ca^{2+}. For instance, Ca^{2+} significantly

396   increased by up to 12% in the 0–15 cm layer of shoulder-slope soils. Across hillslope positions

397   and sampling times, most Ca^{2+} changes were not statistically significant (Tables 1–2). This small

398   Ca^{2+} response likely reflects baseline conditions: Ca^{2+} already dominated exchange sites and little

399   exchangeable acidity was available to neutralize, so displacement of H^+ and Al^{3+} consumed only

400   a small portion of the Ca^{2+} released by basalt dissolution.

401   Compared to Ca^{2+}, the macronutrients Mg^{2+} and K^+ represented a much smaller portion of

402   the soil cation pool and of the basalt feedstock. As a result, changes in Mg^{2+} and K^+ were

403   generally small and statistically insignificant, although Mg^{2+} declined by ~11% and K^+ by 25%

404   along the hayfield shoulder in fall 2023, which may may reflect competitive displacement by

405   Ca^{2+} due to differences in hydration energy and affinity for exchange sites (Anderson, 1989). It

406   should be noted that Mg^{2+} increased by 12.2–18.1% in treated foot slopes at all three post-

407   application samplings, though not significantly.

408   Effects on soil P ranged from –29% to 15.8%, with significant declines limited to the

409   hayfield summit in spring and fall 2024 (–23% and –29%). Increases in pH and Ca^{2+} can

410   precipitate phosphate as calcium-phosphate minerals and reduce anion exchange capacity

411   (Hinsinger et al., 1995). However, low background P concentrations likely limited this

412   mechanism. Additionally, the observed P declines may also reflect reduced manure inputs and

413   plant uptake.

414   Others have reported that P, Mg^{2+}, and K^+ released from basalt dissolution were rapidly

415   taken up by plants, leaving little behind in the soil (Dalmora et al., 2020), but this mechanism

416   remains speculative and warrants further study. The low-grade metamorphism of the basalt likely

417   also controlled the transfer of Mg^{2+} and K^+ to the soil cation pool. As described above, Mg^{2+} is

418   concentrated in metamorphic actinolite and chlorite, while K^+ is a dominant interlayer cation

419   within the alteration product sericite (white mica). These three minerals are more stable in near-

420   surface environments than augite and plagioclase and dissolve more slowly (Goldich, 1938).

421   Overall, our findings contrast with many tropical studies where basalt amendments increase

422   exchangeable nutrient concentrations; in this temperate site, increases were restricted to Ca^{2+} and

423   pH, with inconsistent or negligible effects on Mg^{2+} and K^+. This contrast could also be partly

424   explained by differences in dissolution rates of primary igneous minerals in the tropical basalts

425   versus the metamorphic basalt used here.

Topographic and Land-Use Controls on ERW Response

426

427   Land use and topographic position jointly structured both baseline soil acidity and the

428   magnitude of basalt-induced change. Pasture foot slopes exhibited the lowest baseline pH, while

429   acidity was attenuated at the toe slope. By contrast, hayfield soils (subject to uniform

430   management) were more buffered, with relatively higher and more consistent baseline pH that

431   declined only modestly from summit to shoulder. Within the Sleepers River watershed, previous

432   hydrologic monitoring documented spring snowmelt–driven leaching of base cations from

433   midslopes and redeposition downslope, often enriching toe slopes with Ca^{2+} (McGlynn et al.,

434   1999). This process may partly account for the natural catena pattern at the site, where Ca^{2+} is

435   greater on the toe slope than on the upgradient foot and shoulder slopes, and pH and Ca^{2+} are

436   most depressed on the foot slope, possibly corresponding to the area of greatest cation leaching

437   (Fig. 2). Superimposed on this natural gradient is a land-use shift: pastures dominate the foot and

438   toe slopes, while hayfields occupy the shoulder and summit. Manure inputs from rotational

439   grazing likely amplify acidity in pastures via nitrification of ammonium-rich compounds (Tian &

440   Niu, 2015). The consistent organic matter concentration across the catena and the absence of

441   sulfide oxidation features (Fig. S1; Table S1) support this interpretation, suggesting that

442   differences in organic acids are not the primary driver. Together, these anthropogenic and

443   topographic forces generate a distinct pattern of soil acidity across the landscape, which shapes

444   baseline fertility and constrains the realized effect of basalt application. These catena patterns

445   and their seasonal dynamics are illustrated in the baseline panel of Fig. 4.
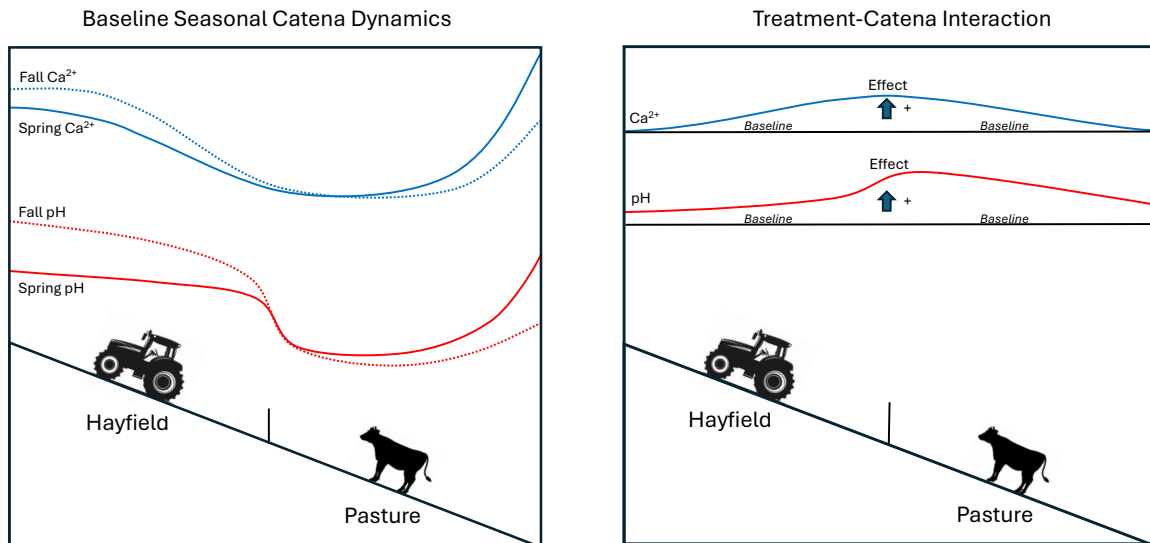
Fig. 4. Seasonal and treatment-mediated soil chemistry gradients along the hayfield-to-pasture catena.
Left panel: Seasonal changes in pH (red) and Ca^{2+} (blue) across slope positions between spring and fall.
Right panel: Basalt-induced changes in pH and Ca^{2+}, with arrows indicating the direction and relative
magnitude of responses by slope position.

Accordingly, the largest basalt-induced pH increases occurred where pre-treatment pH

was lowest. By the final sampling (13 months post-application), pasture foot slopes exhibited the

largest pH rise, slightly exceeding that of the toe slope. Hayfield shoulder slopes (the next-most

acidic plots) also showed clear pH gains, whereas the hayfield summit (which had the highest

baseline pH) showed much weaker or negligible change. Treatment effects on Ca^{2+} were

consistently positive at the pasture foot slope across all three post-application sampling times,

although not statistically significant (likely due to background variability in the pasture).

Exchangeable Ca^{2+} increased significantly at the hayfield shoulder. These parallel increases in

Ca^{2+} at the pasture foot and hayfield shoulder, along with pH rises across all positions, resemble

a liming response, especially since Ca^{2+} increased most where pH rose most. In short, baseline

acidity patterns set by land use and topography governed the magnitude and location of the

462   basalt amendment response, effectively targeting the most acidic areas (Tables 1–2; Tables S3a–

463   S3b). This response across slope positions is depicted in the treatment–catena panel of Fig. 4.

464   Management-induced heterogeneity within the pastures (Fig. 2) may have further

465   obscured treatment signals. Irregular, rotational grazing and localized manure "hot spots" (Penn

466   et al., 2007) likely created a patchy distribution of soil acidity and compaction, inflating the

467   variability of soil properties in the pasture. This is reflected in the wider spread of baseline pH

468   and Ca^{2+} values for pasture plots (Fig. 2). Such spatial noise could mask the effects of basalt,

469   making it difficult to detect significant treatment-induced changes in soil pH even when the

470   mean values were trending upward. Our experimental design, which employed replicated

471   transects spanning different slope positions and land uses, was intended to account for this

472   inherent variability, and it enabled us to discern some treatment effects despite the noise. Still,

473   mitigating the effects that field-level heterogeneity has in lowering statistical precision and

474   power is challenging. Our findings suggest that MRV (measurement, reporting, and verification)

475   strategies for field-scale silicate amendments may require large sample sizes or stratified

476   sampling schemes to reliably detect soil chemistry changes in working landscapes.

477   ## Agronomic implications of enhanced rock weathering

478   The observed rise in soil pH indicates that rock dust could serve as an alternative liming

479   agent at standard agronomic rates in mildly acidic temperate soils, potentially improving nutrient

480   uptake and plant growth. Multi nutrient effects were limited, with only a slight and inconsistent

481   shift toward greater Ca^{2+} dominance in the bioavailable nutrient pool, indicating that basalt

482   amendments alone are unlikely to serve as a comprehensive multi nutrient fertilizer in well

483   buffered temperate soils. Companies focused on carbon sequestration have positioned rock dust

484 co-benefits, increasing referred to as "co-drivers", primarily in terms of their liming value in the

485 United States (Clougherty, 2024; Planavsky et al., 2025). By contrast, in tropical soils where

486 silicate amendments are applied at rates below 50 t ha^{-1}, both pH and exchangeable nutrient

487 levels (e.g., P and K$^+$) can rise sharply, sometimes doubling (Table S5). This regional distinction

488 highlights that silicate amendments act as both fertilizers and liming agents in tropical contexts

489 but primarily as liming agents in temperate environments.

490   Finally, it is important to recognize that the broader adoption of ERW will depend on its

491 agronomic value as much as its climate value. Farmers are more likely to embrace rock dust

492 applications if they observe clear benefits to soil health or crop productivity (Beerling et al.,

493 2020; Swoboda et al., 2022). In this regard, our study offers a reassuring note: the key soil

494 fertility metrics that improved, namely pH and, to a lesser extent, exchangeable essential

495 nutrients, are the very metrics routinely measured in farm soil tests. These standard fertility

496 assays already populate farm records and can readily supply field-scale inputs to drive

497 weathering and carbon-sequestration models (Kanzaki et al., 2025; Kanzaki et al., 2022).

498 Developing MRV frameworks that incorporate such routine soil tests would enable stakeholders

499 to quantify ERW's co-benefits for soil fertility while simultaneously verifying carbon removal,

500 thereby building confidence in the practice from both an agricultural and a climate mitigation

501 perspective.

Conclusions

502

503   This 2.5 year watershed-scale investigation, including 13 months of post-application

504 monitoring, confirms that a single 20 t ha^{-1} application of Ca-rich meta-basalt acts as an effective

505 slow-release liming agent, increasing soil pH by 0.15–0.24 units and exchangeable Ca^{2+} by as

506   much as 12% in the top 15 cm of soil. The alkalinization, driven by silicate weathering, was

507   greatest at the most acidic landscape positions (hayfield shoulders and pasture foot slopes),

508   indicating that the efficiency of ERW can be maximized through targeted application. While

509   providing a valuable source of plant-available Ca^{2+}, the amendment should be viewed primarily

510   as an alternative liming material rather than a multi-nutrient fertilizer in well-buffered temperate

511   soils, since other key nutrients showed negligible or minor changes. We conclude that routine

512   agronomic assays can and should be embedded in MRV frameworks to capture ERW's co-

513   benefits for soil fertility. As ERW deployment scales up, field-derived insights can inform

514   effective site selection, optimize application rates, and guide long-term monitoring strategies.

Acknowledgements

Conflict of interest statement

520   The authors declare no conflicts of interest.

Data availability statement

522   The datasets generated and/or analyzed during the current study are available from the

523   corresponding author upon reasonable request.

References

525   Aksoy, H., & Kavvas, M. L. (2005). A review of hillslope and watershed scale erosion and
526   sediment transport models. *Catena*, *64*(2-3), 247-271.

Amgain, N., Zacharias, Q., Rabbany, A., & Bhadha, J. H. (2021). Effect of sulfur on rice water quality, nutrient uptake, and yields on shallow histosols. *Journal of rice research and Development*, *4*(1), 324-330.

Anda, M., Shamshuddin, J., & Fauziah, C. (2013). Increasing negative charge and nutrient contents of a highly weathered soil using basalt and rice husk to promote cocoa growth under field conditions. *Soil and Tillage Research*, *132*, 1-11.

Anderson, S. J. (1989). *Variable-charge properties of soils containing 2: 1 phyllosilicates*. University of California, Riverside.

Barbier, M., Rabbany, A., & Bhadha, J. H. (2021). Assessing the Effect of Basalt Rock Fines, Activated Humic substances and Its Interaction on Rice Growth and Yield. *Rice Research: OPen Access*.

Beerling, D. J., Epihov, D. Z., Kantola, I. B., Masters, M. D., Reershemius, T., Planavsky, N. J., Reinhard, C. T., Jordan, J. S., Thorne, S. J., & Weber, J. (2024). Enhanced weathering in the US Corn Belt delivers carbon removal with agronomic benefits. *Proceedings of the National Academy of Sciences*, *121*(9), e2319436121.

Beerling, D. J., Kantzas, E. P., Lomas, M. R., Wade, P., Eufrasio, R. M., Renforth, P., Sarkar, B., Andrews, M. G., James, R. H., & Pearce, C. R. (2020). Potential for large-scale CO 2 removal via enhanced rock weathering with croplands. *Nature*, *583*(7815), 242-248.

Bell, D. S., Epihov, D. Z., Dupla, X., Beerling, D., & Leake, J. R. (2024). Enhanced Rock Weathering in Grassland: Benefits and Risks of Basalt Rock Dust to Soils, Forage Production, and Floristic Diversity in a Slightly Acidic Hay Meadow. *Forage Production, and Floristic Diversity in a Slightly Acidic Hay Meadow*.

Blette, V. L., & Newton, R. M. (1996). Effects of watershed liming on the soil chemistry of Woods Lake, New York. *Experimental Watershed Liming Study*, 33-52.

Burbano, D. F. M., Theodoro, S. H., de Carvalho, A. M. X., & Ramos, C. G. (2022). Crushed volcanic rock as soil remineralizer: a strategy to overcome the global fertilizer crisis. *Natural Resources Research*, *31*(5), 2197-2210.

Campbell, N. S. (2009). *The use of rockdust and composted materials as soil fertility amendments* University of Glasgow].

Clougherty, S. (2024). Soil researchers testing basalt rock powder's power as lime alternative. *American Farm Publications*.

Cong, L., Lu, S., Jiang, P., Zheng, T., Yu, Z., & Lü, X. (2024). CO_2 sequestration and soil improvement in enhanced rock weathering: A review from an experimental perspective. *Greenhouse Gases: Science and Technology*, *14*(6), 1122-1138.

Dahlin, A. S., & Stenberg, M. (2017). Effect of wood ash and crushed rock soil amendments on red clover growth and dinitrogen fixation. *Agricultural and Food Science*, *26*(4), 188–197-188–197.

Dalmora, A. C., Ramos, C. G., Oliveira, M. L. S., Oliveira, L. F. S., Schneider, I. A. H., & Kautzmann, R. M. (2020). Application of andesite rock as a clean source of fertilizer for eucalyptus crop: Evidence of sustainability. *Journal of cleaner production*, *256*, 120432.

Dupla, X., Möller, B., Baveye, P. C., & Grand, S. (2023). Potential accumulation of toxic trace elements in soils during enhanced rock weathering. *European Journal of Soil Science*, *74*(1), e13343.

Gillman, G., Burkett, D., & Coventry, R. (2002). Amending highly weathered soils with finely ground basalt rock. *Applied Geochemistry*, *17*(8), 987-1001.

Goldich, S. S. (1938). A study in rock-weathering. *The Journal of Geology*, *46*(1), 17-58.

Gunnarsen, K. C., Jensen, L. S., Gómez-Muñoz, B., Rosing, M. T., & de Neergaard, A. (2019). Glacially abraded rock flour from Greenland: Potential for macronutrient supply to plants. *Journal of Plant Nutrition and Soil Science*, *182*(5), 846-856.

Haque, F., Santos, R. M., & Chiang, Y. W. (2020). CO2 sequestration by wollastonite-amended agricultural soils–An Ontario field study. *International Journal of Greenhouse Gas Control*, *97*, 103017.

Hartmann, J., West, A. J., Renforth, P., Köhler, P., De La Rocha, C. L., Wolf-Gladrow, D. A., Dürr, H. H., & Scheffran, J. (2013). Enhanced chemical weathering as a geoengineering strategy to reduce atmospheric carbon dioxide, supply nutrients, and mitigate ocean acidification. *Reviews of Geophysics*, *51*(2), 113-149.

Hinsinger, P., Bolland, M., & Gilkes, R. (1995). Silicate rock powder: effect on selected chemical properties of a range of soils from Western Australia and on plant growth as assessed in a glasshouse experiment. *Fertilizer research*, *45*, 69-79.

Holzer, I. O., Nocco, M. A., & Houlton, B. (2023). Direct evidence for atmospheric carbon dioxide removal via enhanced weathering in cropland soil. *Environmental Research Communications*.

Hoskins, B., & Ross, D. (2009). Soil sample preparation and extraction. *Recommended Soil Testing Procedures for the Northeastern United States, Northeastern Regional Publication*(493), 3-10.

Kantola, I. B., Blanc-Betes, E., Masters, M. D., Chang, E., Marklein, A., Moore, C. E., von Haden, A., Bernacchi, C. J., Wolf, A., & Epihov, D. Z. (2023). Improved net carbon budgets in the US Midwest through direct measured impacts of enhanced weathering. *Global Change Biology*.

Kanzaki, Y., Planavsky, N., Zhang, S., Jordan, J., Suhrhoff, J., & Reinhard, C. (2025). Soil cation storage is a key control on the carbon removal dynamics of enhanced weathering. *CDRXIV*.

Kanzaki, Y., Zhang, S., Planavsky, N. J., & Reinhard, C. T. (2022). Soil Cycles of Elements simulator for Predicting TERrestrial regulation of greenhouse gases: SCEPTER v0. 9. *Geoscientific Model Development Discussions*, 1-58.

Kauppi, P., Posch, M., Matzner, E., Kauppi, L., & Kaemaeri, J. (1984). Acidification of forest soils: model development and application for analyzing impacts of acidic deposition in Europe.

Larkin, C. S., Andrews, G., Pearce, C. R., Yeong, K. L., Beerling, D., Bellamy, J., Benedick, S., Freckleton, R. P., Goring-Harford, H., & Sadekar, S. (2022). Quantification of CO2 removal in a large-scale enhanced weathering field trial on an oil palm plantation in Sabah, Malaysia. *Frontiers in Climate*, 161.

Lewis, A. L., Sarkar, B., Wade, P., Kemp, S. J., Hodson, M. E., Taylor, L. L., Yeong, K. L., Davies, K., Nelson, P. N., & Bird, M. I. (2021). Effects of mineralogy, chemistry and physical properties of basalts on carbon capture potential and plant-nutrient element release via enhanced weathering. *Applied Geochemistry*, *132*, 105023.

Luchese, A. V., Pivetta, L. A., Batista, M. A., Steiner, F., Giaretta, A. P. d. S., & Curtis, J. C. D. (2021). Agronomic feasibility of using basalt powder as soil nutrient remineralizer. *African Journal of Agricultural Research*, *17*(1), 487-497.

Manning, D. A., Baptista, J., Limon, M. S., & Brandt, K. (2017). Testing the ability of plants to access potassium from framework silicate minerals. *Science of the total environment*, *574*, 476-481.

McGlynn, B., McDonnell, J. J., Shanley, J., & Kendall, C. (1999). Riparian zone flowpath dynamics during snowmelt in a small headwater catchment. *Journal of Hydrology*, *222*(1-4), 75-92.

Moretti, L., Bossolani, J., Crusciol, C., Moreira, A., Micheri, P., Rossi, R., & Imaizumi, C. (2019). Dunite in agriculture: physiological changes, nutritional status and soybean yield. *Communications in Soil Science and Plant Analysis*, *50*(14), 1775-1784.

Nagy, N. M., & Kónya, J. (2007). Study of pH-dependent charges of soils by surface acid–base properties. *Journal of colloid and interface science*, *305*(1), 94-100.

Nahon, D., Colin, F., & Tardy, Y. (1982). Formation and distribution of Mg, Fe, Mn-smectites in the first stages of the lateritic weathering of forsterite and tephroite. *Clay Minerals*, *17*(3), 339-348.

Penn, C. J., Bryant, R. B., Needelman, B., & Kleinman, P. (2007). Spatial distribution of soil phosphorus across selected New York dairy farm pastures and hay fields. *Soil Science*, *172*(10), 797-810.

Planavsky, N., Raymond, P., Bryce, T., Blanks, K., Katchinoff, J., & Yap, M. (2025, 9/25/2025). *Yale Center for Natural Carbon Capture: Research Through Deployment - Session 2* [Panel presentation]. Yale Climate Week, Yale Club of New York, New York, NY, United States.

Plucknett, D. L. (1972). The use of soluble silicates in Hawaiian agriculture.

Ramezanian, A., Dahlin, A. S., Campbell, C. D., Hillier, S., Mannerstedt-Fogelfors, B., & Öborn, I. (2013). Addition of a volcanic rockdust to soils has no observable effects on plant yield and nutrient status or on soil microbial activity. *Plant and Soil*, *367*, 419-436.

Ramos, C. G., dos Santos de Medeiros, D., Gomez, L., Oliveira, L. F. S., Schneider, I. A. H., & Kautzmann, R. M. (2020). Evaluation of soil re-mineralizer from by-product of volcanic rock mining: experimental proof using black oats and maize crops. *Natural Resources Research*, *29*, 1583-1600.

Ross, D. S., & Ketterings, Q. (1995). Recommended methods for determining soil cation exchange capacity. *Recommended soil testing procedures for the northeastern United States*, *493*(101), 62.

Skov, K., Wardman, J., Healey, M., McBride, A., Bierowiec, T., Cooper, J., Edeh, I., George, D., Kelland, M. E., & Mann, J. (2024). Initial agronomic benefits of enhanced weathering using basalt: A study of spring oat in a temperate climate. *Plos one*, *19*(3), e0295031.

Sun, F., Rioux, R. A., Miller-Brown, W. A., Shrestha, B., Shanley, J. B., Planavsky, N. J., Raymond, P. A., & Saiers, J. E. (2025). Long-term trends of streamwater chemistry in an agricultural watershed: Effects of anthropogenic and climatic factors. *Science of the total environment*, *970*, 179017.

Swoboda, P., Döring, T. F., & Hamer, M. (2022). Remineralizing soils? The agricultural usage of silicate rock powders: A review. *Science of the total environment*, *807*, 150976.

Tavares, L. d. F., de Carvalho, A. M. X., Camargo, L. G. B., Pereira, S. G. d. F., & Cardoso, I. M. (2018). Nutrients release from powder phonolite mediated by bioweathering actions. *International Journal of Recycling of Organic Waste in Agriculture*, *7*, 89-98.

te Pas, E. E., Hagens, M., & Comans, R. N. (2023). Assessment of the enhanced weathering potential of different silicate minerals to improve soil quality and sequester CO2. *Frontiers in Climate*, *4*, 954064.

Tian, D., & Niu, S. (2015). A global analysis of soil acidification caused by nitrogen addition. *Environmental Research Letters*, *10*(2), 024019.

665   Vienne, A., Poblador, S., Portillo-Estrada, M., Hartmann, J., Ijiehon, S., Wade, P., & Vicca, S.
666   (2022). Enhanced weathering using basalt rock powder: carbon sequestration, co-benefits
667   and risks in a mesocosm study with Solanum tuberosum. *Frontiers in Climate*, 72.
668   Wang, C., Zhang, G., Zhu, P., Chen, S., & Wan, Y. (2023). Spatial variation of soil functions
669   affected by land use type and slope position in agricultural small watershed. *Catena*, *225*,
670   107029.
671   Wolf, E., & Heard, H. (1983). Response of sugar cane on three P carriers, dolomitic lime and
672   calcium silicate on a hutton in the Natal midlands. Tenth National Congress of the Soil
673   Science Society of Southern Africa, East London, 29 June to 3 July 1981.,
674   Yale Herbarium. (2023). Herbarium catalog of plant species collected by Quinn Zacharias
675   (Catalog Nos. YU.193926–YU.193930). In.
676   Yan, P., Zou, Z., Zhang, J., Yuan, L., Shen, C., Ni, K., Sun, Y., Li, X., Zhang, L., & Zhang, L.
677   (2021). Crop growth inhibited by over-liming in tea plantations. *Beverage Plant*
678   *Research*, *1*(1), 1-7.
679   Yusiharni, B., Ziadi, H., & Gilkes, R. (2007). A laboratory and glasshouse evaluation of chicken
680   litter ash, wood ash, and iron smelting slag as liming agents and P fertilisers. *Soil*
681   *Research*, *45*(5), 374-389.

682

Supplementary Information (SI)

Table of Contents

Hayfield Soil Pit

A

Pasture Soil Pit

B

Fig. S1. Representative soil-pit profiles from Sleepers River subwatershed 2 (W2) (excavated 9 Aug 2023).

(a) Pit 1 – hayfield (44.45993 ° N, 72.09042 ° W; USDA horizon sequence A–E–Bw–BC). A well-drained profile with a thin granular A horizon (0–14 cm; sandy loam by feel test) over a paler E (14–23 cm; loamy sand) and reddish Bw (23–43 cm; sandy loam) that grades to a sandier BC (> 43 cm). Subhedral clinopyroxene-rich saprolite imparts the warm hue; root density declines sharply below 10 cm.

(b) Pit 2 – pasture (44.45937 ° N, 72.09166 ° W; USDA sequence A–ABg–Bg–Cg). A seasonally wet profile with a thicker, dark A horizon (0–20 cm; loam) over mottled ABg/Bg (20–51 cm; clay loam to clay) and a clay-rich, reduced Cg (> 51 cm). Grey matrix colors and rusty mottles indicate periodic saturation.

A folding tape marked in imperial inches provides depth reference (1 in ≈ 2.54 cm); the zero mark is set at the ground surface. Horizon boundaries correspond to the chemical and color data reported in Supplementary Table S1.

Table S1. Morphological color and chemical properties of horizons in two exploratory soil pits.

Pit 1 was excavated in the eastern hayfield (44.45993° N, 72.09042° W) and Pit 2 in an adjacent eastern pasture (44.45937° N, 72.09016° W) on 9 August 2023; laboratory analyses were completed on 8 December 2024. Both pits were hand-dug to ~50 cm. Horizons deeper than 43 cm are reported simply as "> 43 cm" because material below 50 cm was not examined systematically.

Columns list: Pit ID, horizon label, depth interval (cm), Munsell color of moist and dry soil (determined with the Munsell Soil Color Charts, 2009 rev. ed.), organic-matter (OM) content by loss on ignition at 375 °C, and physicochemical properties (pH, ECEC, and extractable nutrients) measured as detailed in the methods section. Depths were recorded with an imperial tape in the field and converted to centimeters (nearest cm). Corresponding pit photographs are provided in Fig. S1.

Pit ID	Horizon	Depth (cm)	Munsell color (dry)	Munsell color (wet)	Soil pH	OM (% WT)	Acidity (meq 100 g^{-1})	ECEC (meq 100 g^{-1})	Ca^{2+} (mg kg^{-1})	Mg^{2+} (mg kg^{-1})	P (mg kg^{-1})	K$^+$ (mg kg^{-1})
Pit 1	A	0-14	2.5y4/3	2.5y3/2	6.42	6.9	0	9.9	1730	115	1.3	57
Pit 1	E	14-23	2.5y4/2.5	2.5y3/2	6.33	4.6	0	6.2	1126	40	0.6	23
Pit 1	Bw	23-43	10yr4/3	10yr3/3	6.23	1.4	0	1.4	227	11	0.3	6.8
Pit 1	Bc	>43	10yr4/3	10yr3/2	5.97	1.4	0	0.8	126	8.1	0.4	7.4
Pit 2	A	0-20	2.5y3/3	2.5y2.5/1	5.67	6.5	0.4	7.9	1378	51	0.6	55
Pit 2	ABg	20-23	2.5y3/2	2.5y3/1	6.25	5.2	0	6.9	1313	23	0.4	30
Pit 2	Bg	23-51	2.5y4/2	2.5y3/2	6.38	6.38	0	4.1	777	10	0.3	22
Pit 2	Cg	>51	2.5y3/1	2.53/1	6.75	6.75	0	10.1	1912	39	0.7	58

Table S2. Basalt feedstock characterization

(a) Major oxide composition and loss on ignition (LOI)

Major Oxides and LOI	Content (%) FUS-ICP Analyses
Silicon dioxide (SiO_2)	51.62
Titanium dioxide (TiO_2)	0.98
Aluminium oxide (Al_2O_3)	13.64
Iron oxide ($Fe_2O_3(T)$)	13.16
Manganese oxide (MnO)	0.20
Magnesium oxide (MgO)	5.77
Calcium oxide (CaO)	9.15
Sodium oxide (Na_2O)	2.98
Potassium oxide (K_2O)	0.87
Phosphorus pentoxide (P_2O_5)	0.13
Loss on Ignition (LOI)	2.29
Total	100.80

(b) Modal mineralogy from thin-section point count

Mineral	Formula	%
Clinopyroxene	$(Ca,Mg,Fe)(Si,Al)_2O_6$	35.1
Plagioclase	$CaAl_2Si_2O_8-NaAlSi_3O_8$	33.7
Sericite	$KAl_2(AlSi_3O10)(OH)_2$	10.6
Chlorite	$(Mg,Al,Fe^{+2})_6(Si,Al)_4O_{10}(OH)_8$	9.2
Actinolite	$Ca_2(Mg,Fe)_5Si8O_{22}(OH)_2$	6.7
Opaque Fe-Ti oxides	$Fe_3O_4-Fe_2TiO_4$	3.8
Quartz	SiO_2	0.9

(c) Basalt feedstock characterization: grain size distribution

Grain Distribution (Sieve Size)	% Passing
#4 (4.75 mm)	100.0
#8 (2.36 mm)	99.1
#10 (2 mm)	98.8
#16 (1.18 mm)	97.7
#30 (0.6 mm)	93.7
#40 (0.425 mm)	89.0
#50 (0.3 mm)	81.4
#60 (0.25 mm)	76.9
#100 (0.15 mm)	61.4
#200 (75 μm)	38.5
Pan	0.00

(d) pH, effective cation exchange capacity (ECEC), and modified Morgan-extractable nutrients of crushed basalt feedstock

Material	pH	ECEC (meq 100 g^{-1})	Ex. Ca^{2+} (mg kg^{-1})	EX. Mg^{2+} (mg kg^{-1})	Ex. P (mg kg^{-1})	Ex. K^{+} (mg kg^{-1})
Feedstock	8.27 ± 0.03	50.1 ± 3.4	9786.33 ± 674.99	116.23 ± 6.62	0.31 ± 0.12	79.47 ± 28.46
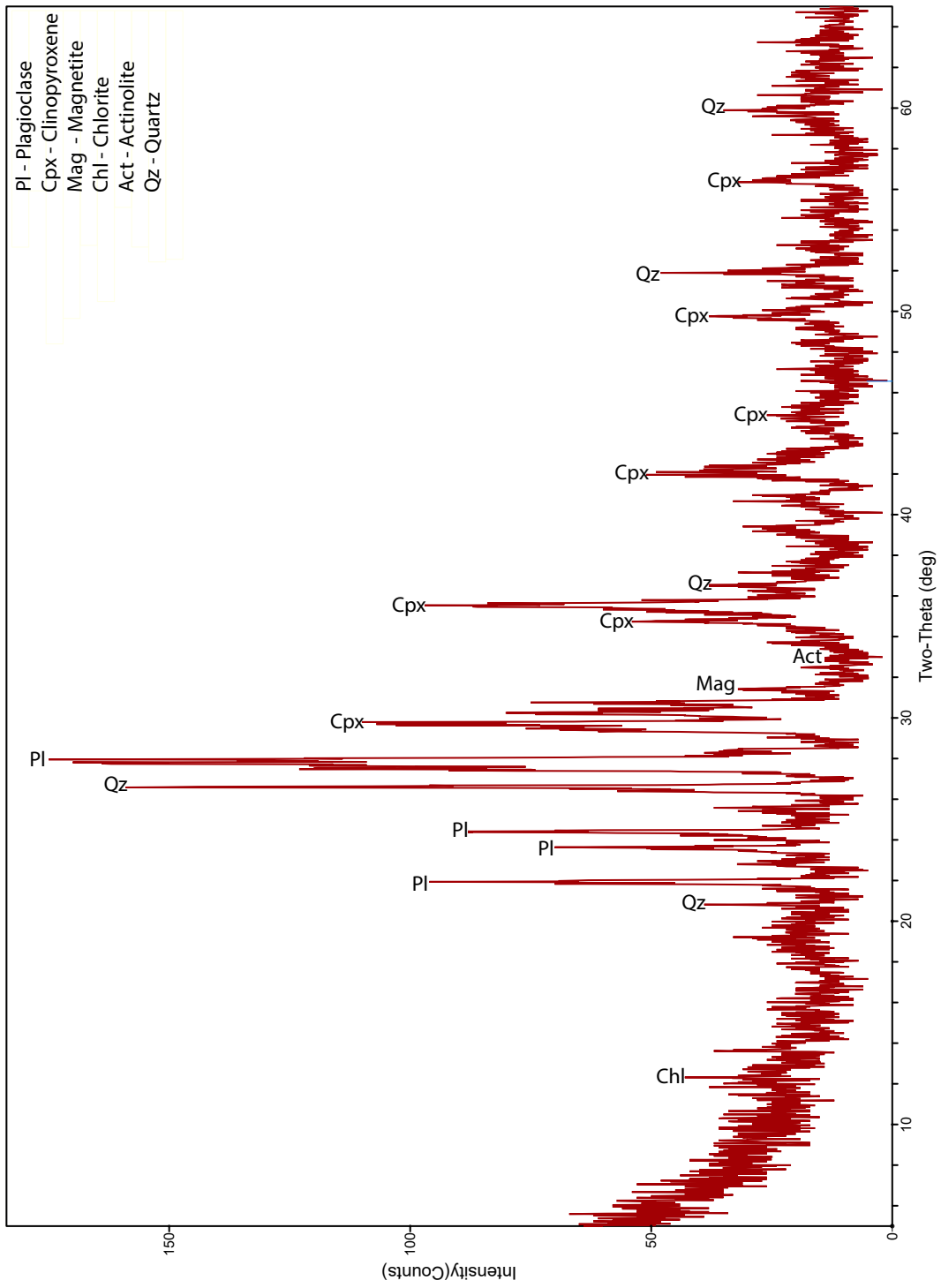
Fig. S2. Powder-X-Ray diffractogram of the crushed Pioneer Valley basalt feedstock acquired on a Rigaku Ultima IV diffractometer (Cu Kα radiation, λ = 1.5418 Å; 43 kV, 35 mA).

The sample mount was rotated at 1 rpm and scanned from 5° to 65° 2θ with a 0.02° step size and 1 s dwell time; the scan was repeated twice and averaged. Diffraction peaks are consistent with clinopyroxene (Cpx), plagioclase (Pl), sericite (Ser), chlorite (Chl), actinolite (Act), magnetite (Mag), titanomagnetite (Ttnmag), titanite (Ttn), quartz (Qz), apatite (Ap), and minor opaque phases (Opq). No calcite or other carbonate reflections were detected, indicating negligible pre-weathering carbonation of the feedstock. Quantitative modal proportions cited in the text (35% Cpx, 34% Pl, 11% Ser, 9% Chl, 7% Act, 4% Opq, 1% Qz) were obtained independently by a 1000-point thin-section count; the XRD pattern shown here is qualitative and was used solely for phase confirmation and carbonate screening.
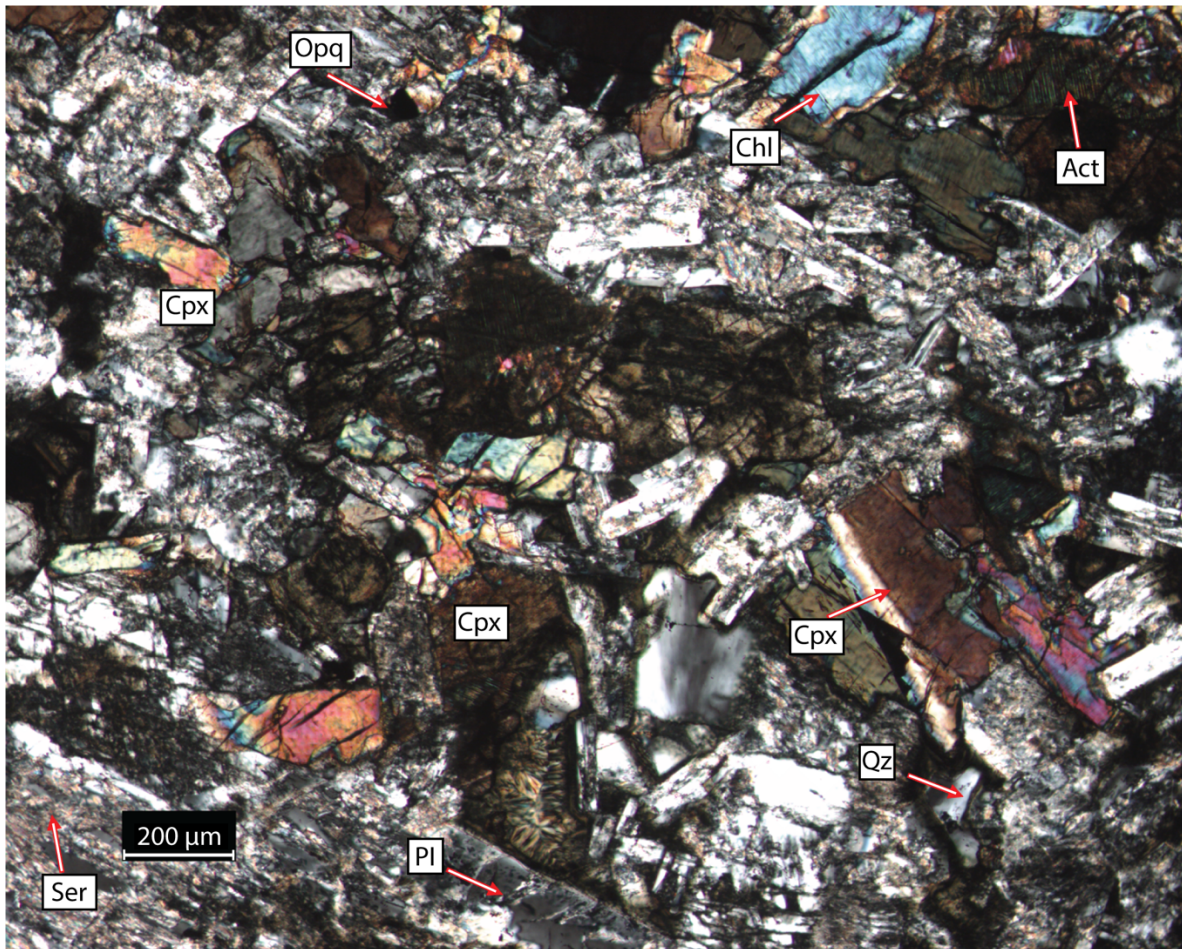
Fig. S3. Cross-polarized photomicrograph of the Pioneer Valley basalt thin section used for the 1000-point modal count (10 × objective; field width ≈ 200 μm).

Subhedral clinopyroxene (Cpx) crystals are partly replaced by actinolite (Act) and chlorite (Chl). Plagioclase (Pl) laths, originally calcic, are variably altered to sodium-rich plagioclase (albite) and sericite (Ser), occurring both as laths and in the groundmass. Sparse quartz (Qz) and opaque Fe–Ti oxide grains (Opg, chiefly titanomagnetite) occupy the groundmass. The thin section thus records partial alteration of clinopyroxene to actinolite ± chlorite and plagioclase to albite ± sericite.

Table S3. Summary statistics for baseline soil-fertility parameters for toe-slope, foot-slope, shoulder-slope, and summit positions

(a) Fall 2022 (baseline)

	pH	ECEC (meq 100 g^{-1})	Base Sat. (%)	Ca^{2+} (mg kg^{-1})	Mg^{2+} (mg kg^{-1})	K$^+$ (mg kg^{-1})	P (mg kg^{-1})	Ex. H$^+$ (%)
Toe Slope (Plots I, II)								
Median	5.8	8.8	98	1565.5	54.4	94.0	1.2	2
Minimum	4.9	4.4	79	750.2	29.0	59.1	0.7	1
Maximum	7.2	17.8	99	3367.9	285.5	556.8	3.5	21
IQR	0.8	5.8	4	1181.2	25.0	90.5	0.4	4
Foot Slope (Plots III, IV)								
Median	5.6	6.3	90	1009.0	61.2	128.1	1.2	10
Minimum	5.3	4.4	73	519.6	37.5	48.8	0.8	0
Maximum	7.5	17.8	100	3397.4	137.8	250.1	2.1	27
IQR	0.3	2.6	10	446.0	29.1	145.4	0.5	10
Shoulder Slope (Plots V, VI)								
Median	6.4	9.4	98	1529.2	136.0	76.5	1.8	2
Minimum	5.7	6.7	92	965.2	107.6	46.5	1.2	1
Maximum	6.6	14.0	99	2531.5	162.5	180.6	3.1	8
IQR	0.3	3.0	1	592.9	36.4	46.1	0.9	1
Summit (Plots VII, VIII)								
Median	6.4	10.7	98	1832.7	116.1	50.4	1.8	2
Minimum	6.0	7.1	97	1211.9	81.0	39.8	1.2	1
Maximum	7.2	16.4	99	2868.4	189.2	111.2	4.9	3
IQR	0.4	2.7	1	581.9	32.4	26.6	1.5	1

(b) Spring 2023 (baseline)

Toe Slope (Plots I, II)							
	pH	ECEC	Base Sat.	Ca^{2+}	Mg^{2+}	K$^+$	P	Ex. H$^+$
		(meq 100 g^{-1})	(%)	(mg kg^{-1})	(mg kg^{-1})	(mg kg^{-1})	(mg kg^{-1})	(%)
Median	5.9	12.1	0.99	2229.3	66.4	92.6	1.5	7.9
Minimum	5.3	6.8	0.82	941.0	41.8	58.5	0.5	4.1
Maximum	7.7	21.5	1.00	4028.2	244.5	452.9	3.3	12.8
IQR	0.6	8.3	0.03	1741.2	41.3	56.3	1.1	2.7
Foot Slope (Plots III, IV)							
	pH	ECEC	Base Sat.	Ca^{2+}	Mg^{2+}	K$^+$	P	Ex. H$^+$
		(meq 100 g^{-1})	(%)	(mg kg^{-1})	(mg kg^{-1})	(mg kg^{-1})	(mg kg^{-1})	(%)
Median	5.6	7.4	0.92	1112.9	66.5	133.0	1.3	7.0
Minimum	5.2	5.3	0.77	633.5	47.0	56.6	0.5	3.8
Maximum	7.7	22.4	1.00	4196.0	140.4	242.8	1.7	9.4
IQR	0.6	4.9	0.17	1161.7	23.5	102.8	0.5	2.2
Shoulder Slope (Plots V, VI)							
	pH	ECEC	Base Sat.	Ca^{2+}	Mg^{2+}	K$^+$	P	Ex. H$^+$
		(meq 100 g^{-1})	(%)	(mg kg^{-1})	(mg kg^{-1})	(mg kg^{-1})	(mg kg^{-1})	(%)
Median	6.2	9.4	0.98	1590.8	129.9	79.3	2.2	6.2
Minimum	5.9	4.8	0.96	794.1	79.3	35.2	1.1	5.1
Maximum	6.8	11.7	0.99	2141.4	177.6	180.5	3.7	8.9
IQR	0.2	1.9	0.01	412.1	22.1	83.8	1.4	0.9
Summit (Plots VII, VIII)							
	pH	ECEC	Base Sat.	Ca^{2+}	Mg^{2+}	K$^+$	P	Ex. H$^+$
		(meq 100 g^{-1})	(%)	(mg kg^{-1})	(mg kg^{-1})	(mg kg^{-1})	(mg kg^{-1})	(%)
Median	6.2	9.6	0.98	1668.1	130.0	70.6	2.2	6.0
Minimum	5.9	7.3	0.96	1170.1	71.2	43.0	1.2	5.2
Maximum	6.9	15.7	0.99	2736.0	191.7	141.8	4.9	7.5
IQR	0.3	2.4	0.01	478.5	18.4	45.5	1.4	1.1

Table S4. Linear mixed-effects model results for soil pH and fertility indicators across hayfield and pasture plots.

Panels (a)–(f) report model estimates for hayfield soils; panels (g)–(l) report results for pasture soils. Each panel includes fixed-effect estimates (β), standard errors (SE), 95% confidence intervals (CI), and p-values for treatment and covariate terms. Percent changes (%Δ) are calculated relative to the model intercept and are shown where applicable. All models include plot as a random effect and are based on spring 2024 post-treatment data collected approximately 13 months after basalt application.

(a) Hayfield pH model results

Hayfield	pH	AIC: -107.85						
Term	β	SE (β-scale)	95% CI (β-scale) Lower	95% CI (β-scale) Upper	% Δ	95% CI (%-scale) Lower	95% CI (%-scale) Upper	p-value
Intercept	6.40	0.06	6.28	6.51	—	—	—	0.00
β_1	−0.06	0.07	−0.21	0.09	—	—	—	0.41
η_2	−0.17	0.03	−0.24	−0.10	—	—	—	0.00
η_3	0.08	0.04	−0.01	0.17	—	—	—	0.07
η_4	−0.09	0.04	−0.18	0.00	—	—	—	0.04
η_5	−0.03	0.04	−0.12	0.06	—	—	—	0.48
α_3	0.10	0.07	−0.03	0.24	—	—	—	0.11
α_4	0.15	0.07	0.02	0.28	—	—	—	0.02
α_5	0.03	0.07	−0.10	0.16	—	—	—	0.61
δ_3	0.11	0.08	−0.04	0.26	—	—	—	0.16
δ_4	0.00	0.08	−0.15	0.15	—	—	—	1.00
δ_5	0.13	0.08	−0.02	0.28	—	—	—	0.09
$\alpha_3 + \delta_3$	0.21	0.06	0.09	0.34	—	—	—	0.00
$\alpha_4 + \delta_4$	0.15	0.06	0.02	0.27	—	—	—	0.02
$\alpha_5 + \delta_5$	0.16	0.06	0.04	0.29	—	—	—	0.01

(b) Hayfield ECEC model results

Hayfield	ECEC	AIC: -155.23						
Term	β	SE (β-scale)	95% CI (β-scale) Lower	95% CI (β-scale) Upper	% Δ	95% CI (%-scale) Lower	95% CI (%-scale) Upper	p-value

Term	β	SE (β-scale)	95% CI (β-scale) Lower	95% CI (β-scale) Upper	% Δ	95% CI (%-scale) Lower	95% CI (%-scale) Upper	p-value
Intercept	2.31	0.05	2.22	2.41	—	—	—	0.00
β_1	−0.07	0.06	−0.19	0.06	−6.3	−17	6	0.31
η_2	−0.04	0.03	−0.09	0.02	−3.5	−9	2	0.22
η_3	−0.02	0.04	−0.10	0.05	−2.1	−9	5	0.56
η_4	−0.05	0.04	−0.13	0.02	−5.1	−12	2	0.16
η_5	−0.11	0.04	−0.19	−0.04	−10.8	−17	−4	0.00
α_3	0.02	0.06	−0.09	0.13	2.1	−9	14	0.71
α_4	−0.05	0.06	−0.16	0.06	−4.6	−15	7	0.40
α_5	−0.04	0.06	−0.15	0.07	−4.0	−14	7	0.47
δ_3	0.05	0.07	−0.08	0.18	5.5	−7	20	0.41
δ_4	0.11	0.07	−0.02	0.24	11.7	−2	27	0.09
δ_5	0.08	0.07	−0.05	0.21	8.5	−5	24	0.22
$\alpha_3 + \delta_3$	0.07	0.05	−0.03	0.18	7.6	−3.2	19.9	0.16
$\alpha_4 + \delta_4$	0.06	0.05	−0.04	0.17	7.0	−4.3	18.5	0.24
$\alpha_5 + \delta_5$	0.04	0.05	−0.07	0.15	4.5	−6.4	15.9	0.45

(c) Hayfield Ca^{2+} model results

Hayfield	Ca^{2+}	AIC: -127.73						
Term	β	SE (β-scale)	95% CI (β-scale) Lower	95% CI (β-scale) Upper	% Δ	95% CI (%-scale) Lower	95% CI (%-scale) Upper	p-value
Intercept	7.46	0.06	7.35	7.57	—	—	—	0.00
β_1	−0.10	0.07	−0.24	0.05	−9.4	−21.7	4.9	0.19
η_2	−0.04	0.03	−0.10	0.03	−3.5	−9.3	2.8	0.26
η_3	−0.02	0.04	−0.10	0.06	−1.9	−9.4	6.2	0.63
η_4	−0.04	0.04	−0.12	0.04	−3.7	−11.0	4.3	0.35
η_5	−0.10	0.04	−0.18	-0.02	−9.3	−16.2	−1.8	0.02
α_3	0.03	0.06	−0.09	0.15	2.9	−8.8	16.1	0.63
α_4	−0.05	0.06	−0.17	0.07	−5.0	−15.8	7.2	0.40
α_5	−0.05	0.06	−0.17	0.07	−4.7	−15.5	7.5	0.43
δ_3	0.09	0.07	−0.05	0.23	9.1	−5.2	25.6	0.22
δ_4	0.13	0.07	−0.01	0.27	14.1	−0.9	31.4	0.06

	β	SE (β-scale)	95% CI (β-scale) Lower	95% CI (β-scale) Upper	% Δ	95% CI (%-scale) Lower	95% CI (%-scale) Upper	p-value
δ_5	0.10	0.07	−0.04	0.25	11.0	−3.6	27.8	0.14
$\alpha_3 + \delta_3$	0.12	0.06	0.00	0.23	12.0	0.0	26.1	0.04
$\alpha_4 + \delta_4$	0.08	0.06	−0.03	0.20	9.1	−3.4	21.7	0.16
$\alpha_5 + \delta_5$	0.06	0.06	−0.06	0.17	6.3	−5.8	18.8	0.33

(d) Hayfield Mg^{2+} model results

Hayfield	Mg^{2+}	AIC: -137.88						
Term	β	SE (β-scale)	95% CI (β-scale) Lower	95% CI (β-scale) Upper	% Δ	95% CI (%-scale) Lower	95% CI (%-scale) Upper	p-value
Intercept	4.81	0.04	4.72	4.90	—	—	—	0.00
β_1	0.10	0.05	−0.01	0.21	10.2	−1.2	23.0	0.09
η_2	−0.02	0.03	−0.09	0.04	−2.2	−8.4	4.3	0.49
η_3	0.05	0.04	−0.04	0.13	4.7	−3.5	13.7	0.26
η_4	−0.11	0.04	−0.19	−0.03	−10.4	−17.4	−2.7	0.01
η_5	−0.13	0.04	−0.21	−0.05	−12.2	−19.1	−4.7	0.00
α_3	−0.03	0.06	−0.15	0.09	−3.1	−14.3	9.6	0.61
α_4	−0.06	0.06	−0.18	0.07	−5.5	−16.4	6.9	0.36
α_5	−0.04	0.06	−0.16	0.09	−3.7	−14.8	8.9	0.54
δ_3	−0.09	0.07	−0.23	0.06	−8.3	−20.6	6.0	0.24
δ_4	0.08	0.07	−0.07	0.22	8.1	−6.4	24.9	0.28
δ_5	0.01	0.07	−0.13	0.16	1.3	−12.3	17.1	0.85
$\alpha_3 + \delta_3$	−0.12	0.06	−0.24	0.00	−11.3	−21.0	0.1	0.05
$\alpha_4 + \delta_4$	0.02	0.06	−0.10	0.14	2.7	−9.1	14.9	0.71
$\alpha_5 + \delta_5$	−0.02	0.06	−0.14	0.09	-2.3	−13.3	9.9	0.68

(e) Hayfield P model results

Hayfield	P	AIC: 48.77						
Term	β	SE (β-scale)	95% CI (β-scale) Lower	95% CI (β-scale) Upper	% Δ	95% CI (%-scale) Lower	95% CI (%-scale) Upper	p-value
Intercept	0.72	0.09	0.53	0.91	—	—	—	0.00

Term	β	SE (β-scale)	95% CI (β-scale) Lower	95% CI (β-scale) Upper	% Δ	95% CI (%-scale) Lower	95% CI (%-scale) Upper	p-value
β_1	0.00	0.12	−0.24	0.25	0.3	−21.4	27.9	0.98
η_2	0.04	0.06	−0.08	0.15	3.8	−7.3	16.4	0.51
η_3	−0.14	0.07	−0.29	0.00	−13.2	−24.9	0.3	0.05
η_4	−0.12	0.07	−0.26	0.03	−11.3	−23.2	2.5	0.10
η_5	−0.17	0.07	−0.31	−0.02	−15.2	−26.6	−2.0	0.02
α_3	−0.18	0.11	−0.40	0.04	−16.3	−32.8	4.1	0.11
α_4	−0.26	0.11	−0.48	−0.04	−22.8	−38.0	−3.9	0.02
α_5	−0.34	0.11	−0.56	−0.13	−29.2	−43.1	−11.8	0.00
δ_3	0.14	0.13	−0.11	0.40	15.3	−10.7	49.0	0.27
δ_4	0.33	0.13	0.07	0.58	38.6	7.3	79.1	0.01
δ_5	0.33	0.13	0.08	0.59	39.6	8.0	80.3	0.01
$\alpha_3 + \delta_3$	−0.04	0.11	−0.25	0.18	−1.0	−22.1	19.4	0.74
$\alpha_4 + \delta_4$	0.07	0.10	−0.14	0.28	15.8	−13.1	31.8	0.51
$\alpha_5 + \delta_5$	−0.01	0.11	−0.23	0.21	10.4	−20.8	23.4	0.92

(f) Hayfield K^+ model results

Hayfield	K^+	AIC: 20.29						
Term	β	SE (β-scale)	95% CI (β-scale) Lower	95% CI (β-scale) Upper	% Δ	95% CI (%-scale) Lower	95% CI (%-scale) Upper	p-value
Intercept	4.04	0.09	3.85	4.23	—	—	—	0.00
β_1	0.21	0.12	−0.04	0.45	22.8	−4.0	57.1	0.11
η_2	0.24	0.05	0.14	0.34	26.7	14.6	40.1	0.00
η_3	0.14	0.06	0.02	0.27	15.5	1.6	31.3	0.03
η_4	0.25	0.06	0.12	0.38	28.4	12.9	45.9	0.00
η_5	0.05	0.06	−0.08	0.18	5.3	−7.3	19.7	0.42
α_3	−0.14	0.10	−0.33	0.06	−12.8	−28.3	5.9	0.16
α_4	0.09	0.10	−0.10	0.29	9.9	−9.6	33.6	0.34
α_5	0.05	0.10	−0.14	0.25	5.4	−13.3	28.1	0.59
δ_3	−0.13	0.11	−0.35	0.10	−12.0	−29.9	10.5	0.26
δ_4	−0.15	0.11	−0.37	0.08	−13.7	−31.3	8.3	0.20
δ_5	−0.18	0.11	−0.41	0.05	−16.4	−33.4	4.9	0.12

$\alpha_3 + \delta_3$	−0.26	0.09	−0.45	−0.08	−24.8	−36.4	−7.5	0.00
$\alpha_4 + \delta_4$	−0.05	0.09	−0.24	0.14	−3.8	−21.5	14.5	0.57
$\alpha_5 + \delta_5$	−0.13	0.09	−0.31	0.06	−11.0	−27.0	6.3	0.18

(g) Pasture pH model results

Pasture	pH	AIC: 72.67						
Term	β	SE (β-scale)	95% CI (β-scale) Lower	95% CI (β-scale) Upper	% Δ	95% CI (%-scale) Lower	95% CI (%-scale) Upper	p-value
Intercept	5.72	0.13	5.45	5.99	—	—	—	0.00
β_1	0.32	0.18	−0.05	0.68	—	—	—	0.09
η_2	0.05	0.06	−0.06	0.17	—	—	—	0.36
η_3	0.32	0.07	0.18	0.47	—	—	—	0.00
η_4	0.18	0.07	0.03	0.32	—	—	—	0.01
η_5	0.19	0.07	0.04	0.33	—	—	—	0.01
α_3	0.07	0.110	−0.15	0.29	—	—	—	0.52
α_4	0.19	0.110	−0.03	0.41	—	—	—	0.08
α_5	0.24	0.110	0.02	0.46	—	—	—	0.03
δ_3	0.00	0.128	−0.26	0.26	—	—	—	1.00
δ_4	−0.03	0.128	−0.28	0.23	—	—	—	0.84
δ_5	−0.04	0.128	−0.29	0.22	—	—	—	0.76
$\alpha_3 + \delta_3$	0.07	0.105	−0.14	0.28	—	—	—	0.50
$\alpha_4 + \delta_4$	0.17	0.106	−0.04	0.38	—	—	—	0.11
$\alpha_5 + \delta_5$	0.20	0.106	−0.01	0.41	—	—	—	0.06

(h) Pasture ECEC model results

Pasture	ECEC	AIC: 17.90						
Term	β	SE (β-scale)	95% CI (β-scale) Lower	95% CI (β-scale) Upper	% Δ	95% CI (%-scale) Lower	95% CI (%-scale) Upper	p-value
Intercept	2.00	0.02	1.95	2.04	—	—	—	0.00
β_1	0.39	0.03	0.34	0.44	47.7	39.8	56.0	0.01

	β	SE (β-scale)	95% CI (β-scale) Lower	95% CI (β-scale) Upper	% Δ	95% CI (%-scale) Lower	95% CI (%-scale) Upper	p-value
η_2	0.10	0.01	0.07	0.12	10.3	7.6	13.1	0.04
η_3	0.12	0.02	0.09	0.15	12.6	9.0	16.2	0.06
η_4	0.16	0.02	0.13	0.19	17.5	13.8	21.3	0.01
η_5	0.00	0.02	−0.03	0.03	0.1	−3.0	3.4	0.98
α_3	0.02	0.02	−0.03	0.07	2.3	−2.6	7.3	0.81
α_4	0.00	0.02	−0.05	0.04	−0.4	−5.1	4.6	0.97
α_5	−0.04	0.02	−0.09	0.01	−3.9	−8.5	0.9	0.67
δ_3	−0.07	0.03	−0.13	−0.01	−6.7	−11.8	−1.2	0.52
δ_4	−0.16	0.03	−0.22	−0.11	−15.1	−19.8	−10.2	0.13
δ_5	−0.02	0.03	−0.07	0.04	−1.5	−6.9	4.2	0.89
$\alpha_3 + \delta_3$	−0.05	0.09	−0.23	0.13	−4.4	−20.2	14.2	0.60
$\alpha_4 + \delta_4$	−0.17	0.09	−0.35	0.01	−15.5	−29.3	1.1	0.06
$\alpha_5 + \delta_5$	−0.06	0.09	−0.23	0.12	−5.4	−20.9	13.2	0.54

(i) Pasture Ca^{2+} model results

Pasture	Ca^{2+}	AIC: 62.85						
Term	β	SE (β-scale)	95% CI (β-scale) Lower	95% CI (β-scale) Upper	% Δ	95% CI (%-scale) Lower	95% CI (%-scale) Upper	p-value
Intercept	7.05	0.13	6.79	7.30	—	—	—	0.00
β_1	0.49	0.17	0.14	0.84	62.7	14.7	130.8	0.01
η_2	0.11	0.05	0.00	0.22	11.3	−0.3	24.2	0.05
η_3	0.16	0.07	0.02	0.30	17.7	2.3	35.4	0.02
η_4	0.18	0.07	0.04	0.32	20.0	4.3	38.0	0.01
η_5	0.04	0.07	−0.10	0.18	4.4	−9.2	20.1	0.54
α_3	0.05	0.11	−0.16	0.27	5.5	−14.9	30.7	0.62
α_4	0.05	0.11	−0.17	0.26	4.7	−15.5	29.7	0.67
α_5	0.01	0.11	−0.20	0.22	1.0	−18.5	25.1	0.93
δ_3	−0.10	0.12	−0.35	0.15	−9.6	−29.4	15.9	0.42
δ_4	−0.21	0.12	−0.45	0.04	−18.6	−36.5	4.3	0.10
δ_5	−0.07	0.12	−0.32	0.18	−6.8	−27.3	19.4	0.57
$\alpha_3 + \delta_3$	−0.05	0.10	−0.25	0.16	−4.1	−22.4	17.2	0.65

$\alpha_4 + \delta_4$	−0.16	0.10	−0.37	0.05	−13.9	−30.6	4.7	0.12
$\alpha_5 + \delta_5$	−0.06	0.10	−0.27	0.15	−5.8	−23.4	15.6	0.55

(j) Pasture Mg^{2+} model results

Pasture	Mg^{2+}	AIC: 64.70						
Term	β	SE (β-scale)	95% CI (β-scale) Lower	95% CI (β-scale) Upper	% Δ	95% CI (%-scale) Lower	95% CI (%-scale) Upper	p-value
Intercept	4.12	0.10	3.92	4.32	—	—	—	0.00
β_1	0.12	0.13	−0.14	0.37	12.3	−13.1	44.9	0.37
η_2	0.10	0.06	−0.02	0.22	10.9	−1.7	25.1	0.09
η_3	0.05	0.08	−0.10	0.21	5.6	−9.4	23.0	0.48
η_4	−0.09	0.08	−0.24	0.07	−8.3	−21.3	6.8	0.26
η_5	−0.18	0.08	−0.33	−0.03	−16.4	−28.3	−2.6	0.02
α_3	0.12	0.12	−0.12	0.35	12.2	−11.0	41.4	0.32
α_4	0.17	0.12	−0.07	0.40	18.1	−6.4	48.8	0.15
α_5	0.11	0.12	−0.12	0.35	12.2	−11.0	41.4	0.32
δ_3	−0.22	0.14	−0.49	0.05	−19.8	−38.8	5.1	0.11
δ_4	−0.33	0.14	−0.60	−0.06	−28.1	−45.2	−5.9	0.02
δ_5	−0.11	0.14	−0.38	0.16	−10.8	−31.9	16.9	0.40
$\alpha_3 + \delta_3$	−0.11	0.11	−0.33	0.12	−7.6	−27.9	12.4	0.34
$\alpha_4 + \delta_4$	−0.16	0.11	−0.39	0.06	−10.1	−32.0	5.9	0.14
$\alpha_5 + \delta_5$	0.00	0.23	−0.46	0.46	1.4	−36.6	57.8	1.00

(k) Pasture soil P model results

Pasture	P	AIC: 114.26						
Term	β	SE (β-scale)	95% CI (β-scale) Lower	95% CI (β-scale) Upper	% Δ	95% CI (%-scale) Lower	95% CI (%-scale) Upper	p-value
Intercept	0.21	0.11	0.00	0.42	—	—	—	0.04
β_1	0.18	0.13	−0.09	0.44	19.4	−8.3	55.5	0.19
η_2	−0.02	0.07	−0.17	0.12	−2.4	−15.8	13.2	0.75

η_3	−0.54	0.09	−0.73	−0.35	−41.8	−51.7	−29.9	0.00
η_4	−0.63	0.09	−0.81	−0.44	−46.6	−55.7	−35.6	0.00
η_5	−0.49	0.09	−0.68	−0.31	−39.0	−49.4	−26.5	0.00
α_3	0.05	0.14	−0.23	0.33	5.4	−20.4	39.5	0.71
α_4	−0.07	0.14	−0.35	0.21	−6.6	−29.4	23.7	0.63
α_5	−0.13	0.14	−0.41	0.15	−12.2	−33.7	16.2	0.35
δ_3	−0.11	0.16	−0.44	0.22	−10.2	−35.4	24.7	0.51
δ_4	−0.17	0.16	−0.50	0.16	−15.7	−39.3	17.1	0.30
δ_5	−0.05	0.17	−0.39	0.29	−4.9	−32.2	33.4	0.77
$\alpha_3 + \delta_3$	−0.06	0.14	−0.33	0.22	−4.8	−27.8	24.1	0.68
$\alpha_4 + \delta_4$	−0.24	0.13	−0.51	0.03	−22.3	−39.9	3.1	0.08
$\alpha_5 + \delta_5$	−0.18	0.14	−0.46	0.10	−17.1	−37.0	10.5	0.20

(l) Pasture soil K^+ model results

Pasture	K^+	AIC: 132.56						
Term	β	SE (β-scale)	95% CI (β-scale) Lower	95% CI (β-scale) Upper	% Δ	95% CI (%-scale) Lower	95% CI (%-scale) Upper	p-value
Intercept	4.76	0.12	4.52	5.01	—	—	—	0.00
β_1	−0.09	0.16	−0.42	0.23	−8.8	−34.1	26.1	0.57
η_2	0.04	0.08	−0.11	0.20	4.6	−10.0	21.6	0.55
η_3	−0.05	0.10	−0.24	0.14	−4.7	−21.2	15.4	0.62
η_4	0.09	0.10	−0.10	0.28	9.7	−9.4	32.8	0.33
η_5	−0.05	0.10	−0.24	0.14	−5.0	−21.5	15.0	0.59
α_3	0.03	0.14	−0.26	0.32	2.8	−23.0	37.3	0.85
α_4	−0.17	0.14	−0.46	0.12	−15.5	−36.7	12.8	0.25
α_5	−0.14	0.14	−0.43	0.15	−13.1	−34.9	16.1	0.33
δ_3	−0.14	0.17	−0.48	0.20	−13.0	−37.9	21.9	0.41
δ_4	−0.07	0.17	−0.41	0.27	−6.7	−33.4	30.6	0.68
δ_5	0.14	0.17	−0.20	0.47	14.5	−18.2	60.5	0.42
$\alpha_3 + \delta_3$	−0.11	0.14	−0.39	0.16	−10.1	−32.1	17.9	0.42
$\alpha_4 + \delta_4$	−0.24	0.14	−0.51	0.04	−22.2	−40.2	3.9	0.08

$\alpha_5 + \delta_5$	0.00	0.12	−0.24	0.24	1.5	−21.7	26.6	0.97

Table S5. Comparative Literature Analysis

Purpose of the Table

The primary goals of this table are to:
1. Compare the results of this study to others in the literature,
2. Illustrate the substantial differences in treatment effects between temperate and tropical soils, and
3. Highlight the wide variety of methods used to determine soil fertility indicators.

Data Selection

- We chose a representative set of 10 studies, rather than compiling an exhaustive list, to clearly illustrate overall trends in enhanced rock weathering outcomes under contrasting climate and soil conditions. This focused approach keeps the table concise while showcasing the most relevant distinctions between temperate and tropical systems. Additional references supporting these observations are discussed in the main text.
- Treatment effects (Tables 1–2) from the fall 2023 (three months post-application; upper coefficient) and fall 2024 (13 months post-application; lower coefficient) sampling periods were used to quantify treatment effects at the hayfield summit, hayfield shoulder, pasture foot slope, and pasture toe slope, and to benchmark those effects against values reported in the literature.

Data Presentation and Comparability

- **Calculated Values**: To ensure comparability across studies, absolute changes in pH and percentage changes in CEC and base cations were calculated.
- **Visual Representation**: Two color gradient schemes represent application rates and soil fertility response changes. For W2, shading is based on whichever treatment coefficient, three months or thirteen months post-application, has the larger absolute value (i.e., lies farthest from zero).
- **Data Extraction**: Values extracted using plot digitizer software are indicated in *italics*.
- **Significant Effects**: Treatment effects are **bolded** if they were:
  - Reported as significant in the source study,
  - Exceeded twice the standard deviation of the control.

Annotations and Methods

- **pH Measurement Methods**:
  - pH values determined using the following methods are represented by:
    - i: 1:1 water dilution,
    - ii: 1:2.5 water dilution,
    - iii: 0.02 M $CaCl_2$, or
    - iv: In situ pH probe.
- **Exchangeable Base Cation Extraction Methods**:
  - Letters denote extraction methods:
    - a: Ammonium acetate,
    - b: EDTA,
    - c: Mehlich 1,
    - d: 1 M KCl,
    - e: Mehlich 3,
    - f: 2% citric acid,
    - g: 0.43 M HNO_3,
    - h: 1 M NH_4,
    - j: Modified Morgan.
- **CEC Subdivisions**:
  - CEC measurements are categorized as:
    - I: Included Al,
    - II: Excluded Al, or
    - III: Used ECEC.
- **Unavailable Data**: Cells marked as NA indicate data that was not available.

Region	Source	Field/Lab	Soil Texture & pH	Rock Type	App. Rate (t/ha)	Post App. (months)	pH (Δ)	CEC (%)	Ca (%)	Mg (%)	P (%)	K (%)
W2 (This Study)	Hayfield Summit	Field	Loam (6.4)	Basalt	20	3 & 13	+0.10 +0.03 i	+2 −4 III	+3 −5 j	+3 −6 j	−16.3 −23 j	−12.8 +10 j
	Hayfield Shoulder	Field	Loam (6.3)	Basalt	20	3 & 13	+0.21 +0.16 i	+8 +5 III	+12 +6 j	−11 −2 j	−1 −10 j	−25 −11 j
	Pasture Foot	Field	Loam (5.7)	Basalt	20	3 & 13	+0.07 +0.24 i	+2 −4 III	+5 +1 j	+12 +12 j	+5 −12 j	+3 −13 j
	Pasture Toe	Field	Loam (6.0)	Basalt	20	3 & 13	+0.07 +0.20 i	−4 −5 III	−4 −6 j	−8 +1 j	−5 −17 j	−10 +2 j
Temperate	Dahlin et al. (2014)	Lab	Silt loam (5.4)	Pyroxene Andesite	50	14	0 iii	NA	+1 b	+38 b	+4 b	+5 b
	Dahlin et al. (2017)	Lab	Silt loam (4.8)	Pyroxene Andesite	50	14	0 iii	NA	+1 b	+38 b	+4 b	+5 b
	Vienne et al. (2022)	Lab	Loam (7.7)	Basalt	50	3	NA	+35 II	+13 a	+40 a	NA	+7.1 a
	Te Pas et al. (2023)	Lab	Sand (5.16)	Basalt	>100	2	0.3 iv	+30 II	+56 g	+558 g	NA	+200 g
	Dupla et al. (2024)	Field (0-10 cm)	Loam (6.2-7.5)	Basalt	20	12	+0.09 ii	−3 III	−5 h	+18.7 h	NA	+8 h
Tropical	Anda et al. (2013)	Lab	Clayey (4.0)	Basalt	20	24	+0.67 iv	+79 I	NA	NA	NA	NA
	Ramos et al. (2019)	Lab	Clayey (5.2)	Dacite	18	2.5	+0.05 i	+10 I	+3 d	+10 d	+25 c	+29 c
	Dalmora et al. (2020)	Field (0-20 cm)	Clayey (Na)	Vesicular Andesite	6.6	9	NA	NA	NA	NA	+79 e	+248 e
	Vaghetti Luchhese et al. (2021)	Lab	Sandy clay loam (7.0)	Basalt	33	2.5	+0.24 iii	NA	+9 d	−8 d	+263 d	−1 d
	Burbano et al. (2022)	Lab	(5.4)	Basalt Andisol	23.5	12	NA	NA	NA	+12 d	+90 f	+22 f